

# Jet Production by Virtual Photons

Christer Friberg<sup>1</sup> and Torbjörn Sjöstrand<sup>2</sup>

*Department of Theoretical Physics,  
Lund University, Lund, Sweden*

## Abstract

The production of jets is studied in collisions of virtual photons,  $\gamma^*p$  and  $\gamma^*\gamma^*$ , specifically for applications at HERA and LEP2. Photon flux factors are convoluted with matrix elements involving either direct or resolved photons and, for the latter, with parton distributions of the photon. Special emphasis is put on the range of uncertainty in the modeling of the resolved component. The resulting model is compared with existing data.

---

<sup>1</sup>christer@thep.lu.se

<sup>2</sup>torbjorn@thep.lu.se

# 1 Introduction

The photon is a complicated object to describe. In the DIS region, i.e. when it is very virtual, it can be considered as devoid of any internal structure, at least to first approximation. In the other extreme, the total cross section for real photons is dominated by the resolved component of the wave function, where the photon has fluctuated into a  $q\bar{q}$  state. The nature of this resolved component is still not well understood, especially not the way in which it dies out with increasing photon virtuality. This dampening is likely not to be a simple function of virtuality, but to depend on the physics observable being studied, i.e. on the combination of subprocesses singled out.

Since our current understanding of QCD does not allow complete predictability, one sensible approach is to base ourselves on QCD-motivated models, where a plausible range of uncertainty can be explored. Hopefully comparisons with data may then help constrain the correct behaviour. The ultimate goal therefore clearly is to have a testable model for all aspects of the physics of  $\gamma^*p$  and  $\gamma^*\gamma^*$  collisions. As a stepping stone towards constructing such a framework, in this paper we explore the physics associated with the production of ‘high- $p_\perp$ ’ jets in the collision. That is, we here avoid the processes that only produce activity along the  $\gamma^*p$  or  $\gamma^*\gamma^*$  collision axis. For resolved photons this corresponds to the ‘soft’ or ‘low- $p_\perp$ ’ events of the hadronic physics analogy, for direct ones to the lowest-order DIS process  $\gamma^*q \rightarrow q$ .

The processes that we will study here instead can be exemplified by  $\gamma^*\gamma^* \rightarrow q\bar{q}$  (direct),  $\gamma^*g \rightarrow q\bar{q}$  (single-resolved for  $\gamma^*\gamma^*$ , direct for  $\gamma^*p$ ) and  $gg \rightarrow q\bar{q}$  (double-resolved for  $\gamma^*\gamma^*$ , (single-)resolved for  $\gamma^*p$ ), where the gluons come from the parton content of a resolved virtual photon or from the proton. Note that these are multi-scale processes, at least involving the virtuality  $Q_i^2$  of either photon ( $i = 1, 2$ ) and the  $p_\perp^2$  of the hard subprocess. (In  $\gamma^*\gamma^*$  physics the notation  $P^2$  is often used instead of  $Q^2$ , especially for the less virtual of the two photons; here we will use  $Q^2$  throughout, however.) For a resolved photon, the relative transverse momentum  $k_\perp$  of the initial  $\gamma^* \rightarrow q\bar{q}$  branching provides a further scale, at least in our framework. This plethora of scales clearly is a challenge to any model builder, but in principle it also offers the opportunity to explore QCD in a more differential fashion than is normally possible.

At large photon virtualities, a possible strategy would be to express the cross sections entirely in terms of processes involving the photon directly, i.e. to include branchings such as  $\gamma^* \rightarrow q'\bar{q}'$  and  $q' \rightarrow q'g$  in the Feynman graphs calculated to describe the process, so that e.g. the  $\gamma^*p$  process  $gg \rightarrow q\bar{q}$  is calculated as  $\gamma^*g \rightarrow q'\bar{q}'q\bar{q}$ . With decreasing virtuality of the photon, such a fixed-order approach is increasingly deficient by its lack of the large logarithmic corrections generated by collinear and soft gluon emission, however. Furthermore, almost real photons allow long-lived  $\gamma^* \rightarrow q\bar{q}$  fluctuations, that then take on the properties of non-perturbative hadronic states, specifically of vector mesons such as the  $\rho^0$ . It is therefore that an effective description in terms of parton distributions becomes necessary. Hence the resolved component of the photon, as opposed to the direct one.

That such a subdivision is more than a technical construct is excellently illustrated by the  $x_\gamma^{\text{obs}}$  plots from HERA [1]. This variable sums up the fraction of the original photon light-cone momentum carried by the two highest- $E_\perp$  jets. A clear two-component structure is visible. The peak close to  $x_\gamma^{\text{obs}} = 1$  can be viewed as a smeared footprint of the direct photon, with all the energy partaking in the hard interaction, while the broad spectrum at lower  $x_\gamma^{\text{obs}}$  is consistent with the resolved photon, where much of the energy remains in a beam jet. The distinction between the two is not unique when higher-order

effects are included, but it is always possible to make a functional separation that avoids double-counting or gaps.

The resolved photon can be further subdivided into low-virtuality fluctuations, which then are of a nonperturbative character and can be represented by a set of vector mesons, and high-virtuality ones that are describable by perturbative  $\gamma^* \rightarrow q\bar{q}$  branchings. The former is called the VMD (vector meson dominance) component and the latter the anomalous one. The parton distributions of the VMD component are unknown from first principles, and thus have to be based on reasonable ansätze, while the anomalous ones are perturbatively predictable. This separation is more ambiguous and less well tested than the one between direct and resolved photons. In principle, studies on the structure of the beam remnant, e.g. its  $p_\perp$  distribution, should show characteristic patterns. Unfortunately, the naively expected differences are smeared by higher-order QCD corrections (especially initial-state radiation), by the possibility of multiple parton-parton interactions, by hadronization effects, and so on. (Experimentally, gaps in the detector acceptance, e.g. for the beam pipe, is a further major worry.) Many of these areas offer interesting challenges in their own right; e.g. the way in which multiple interactions die out with virtuality, both that of the photon itself and that of the  $q\bar{q}$  pair it fluctuates to. Models for one aspect at the time are therefore likely to be inadequate. Instead we here attempt a combined description of all the relevant physics topics.

The traditional tool for handling such complex issues is the Monte Carlo approach. Our starting point is the model for real photons [2] and the parton distribution parameterizations of real and virtual photons [3] already present in the PYTHIA [4] generator. Several further additions and modifications have been made to model virtual photons, as will be described in the following. Other generators with an overlapping scope include, among others, HERWIG [5], LDC [6], LEPTO [7], PHOJET [8] and RAPGAP [9]. The details of the approaches are different, however, so this gives healthy possibilities to compare and learn. Another alternative is provided by matrix-element calculations [10], that do not provide the same complete overview but can offer superior descriptions for some purposes.

The plan of this paper is the following. In section 2 the model is described, with special emphasis on those aspects that are new compared with the corresponding description for real photons. Thereafter, in section 3, the dependence of simple observables on model parameters is illustrated. Comparisons are shown with some sets of data from ep and  $e^+e^-$  colliders, and this is used to constrain partly the freedom in the model. Based on this experience, some further observables are then proposed and studied, to help shed light on the nature of the virtual photon. Finally, section 4 contains a summary and outlook.

## 2 The Model

The electromagnetic field surrounding a moving electron can be viewed as a flux of photons. Weizsäcker [11] and Williams [12] calculated the spectrum of these photons, neglecting the photon virtualities and terms involving the longitudinal polarization of photons. This approximation is well-known [13] to be a good approximation when the scattered lepton is tagged at small scattering angles.

In the equivalent photon approximation [14], the cross sections for the processes  $ep \rightarrow e\mathbf{X}$  and  $ee \rightarrow ee\mathbf{X}$ , where  $\mathbf{X}$  is an arbitrary final state, can then be written as the

convolutions

$$d\sigma(ep \rightarrow e\mathbf{X}) = \int \frac{d\omega}{\omega} N(\omega) d\sigma(\gamma p \rightarrow \mathbf{X}) \quad (1)$$

and

$$d\sigma(ee \rightarrow ee\mathbf{X}) = \iint \frac{d\omega_1}{\omega_1} \frac{d\omega_2}{\omega_2} N(\omega_1) N(\omega_2) d\sigma(\gamma\gamma \rightarrow \mathbf{X}) , \quad (2)$$

where  $\omega$  is the energy of the emitted photon. In this approximation, the distribution in photon frequencies  $N(\omega)d\omega/\omega$  is obtained by integrating over the photon virtuality  $Q^2$ . The maximum value  $Q_{\max}^2$  is usually given by experimental conditions like anti-tagging, i.e. that the scattered lepton is not detected if its scattering angle is too small.

A better approximation, and the one used in our approach, is to keep the  $Q^2$  dependence in the photon flux  $f(y, Q^2)$  (with  $y \approx \omega/\omega_{\max}$ , see below) and in the subprocess cross sections involving the virtual photon(s),  $\gamma^* p \rightarrow \mathbf{X}$  and  $\gamma^* \gamma^* \rightarrow \mathbf{X}$ , and to sum over the transverse and longitudinal photon polarizations. Equations (1) and (2) then modify to

$$d\sigma(ep \rightarrow e\mathbf{X}) = \sum_{\xi=T,L} \iint dy dQ^2 f_{\gamma/e}^{\xi}(y, Q^2) d\sigma(\gamma_{\xi}^* p \rightarrow \mathbf{X}) \quad (3)$$

and

$$d\sigma(ee \rightarrow ee\mathbf{X}) = \sum_{\xi_1, \xi_2=T,L} \iiint dy_1 dQ_1^2 dy_2 dQ_2^2 f_{\gamma/e}^{\xi_1}(y_1, Q_1^2) f_{\gamma/e}^{\xi_2}(y_2, Q_2^2) d\sigma(\gamma_{\xi_1}^* \gamma_{\xi_2}^* \rightarrow \mathbf{X}) . \quad (4)$$

For ep events, this factorized ansatz is perfectly general, so long as azimuthal distributions in the final state are not studied in detail. In  $e^+e^-$  events, it is not a good approximation when the virtualities  $Q_1^2$  and  $Q_2^2$  of both photons become of the order of the squared invariant mass  $W^2$  of the colliding photons [15]. In this region the cross section have terms that depend on the relative azimuthal angle of the scattered leptons, and the transverse and longitudinal polarizations are non-trivially mixed. However, these terms are of order  $Q_1^2 Q_2^2 / W^2$  and can be neglected whenever at least one of the photons has low virtuality compared to  $W^2$ .

## 2.1 The Photon Flux

When  $Q^2/W^2$  is small, one can derive [16, 14, 15]

$$f_{\gamma/l}^T(y, Q^2) = \frac{\alpha_{\text{em}}}{2\pi} \left( \frac{(1 + (1-y)^2)}{y} \frac{1}{Q^2} - \frac{2m_l^2 y}{Q^4} \right) , \quad (5)$$

$$f_{\gamma/l}^L(y, Q^2) = \frac{\alpha_{\text{em}}}{2\pi} \frac{2(1-y)}{y} \frac{1}{Q^2} , \quad (6)$$

where  $l = e^{\pm}, \mu^{\pm}$  or  $\tau^{\pm}$ . In  $f_{\gamma/l}^T$  the second term, proportional to  $m_l^2/Q^4$ , is not leading log and is therefore often omitted. Clearly it is irrelevant at large  $Q^2$ , but around the lower cut-off  $Q_{\min}^2$  it significantly dampens the small- $y$  rise of the first term. Overall, under realistic conditions, it reduces event rates by 5–10% [15, 17].

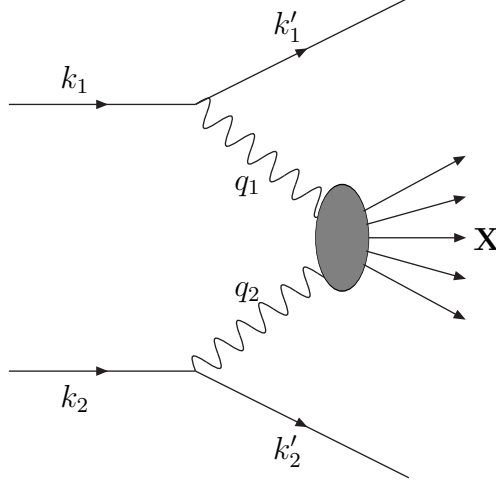


Figure 1: Schematic figure of  $\gamma\gamma$  processes, illustrating the notation.

The  $y$  variable is defined as the light-cone fraction the photon takes of the incoming lepton momentum. For instance, for  $l^+l^-$  events, Fig. 1,

$$y_i = \frac{q_i k_j}{k_i k_j}, \quad j = 2(1) \text{ for } i = 1(2). \quad (7)$$

Alternatively, the energy fraction the photon takes in the rest frame of the collision can be used,

$$x_i = \frac{q_i(k_1 + k_2)}{k_i(k_1 + k_2)}, \quad i = 1, 2. \quad (8)$$

The two are simply related,

$$y_i = x_i + \frac{Q_i^2}{s}, \quad (9)$$

with  $s = (k_1 + k_2)^2$ . (Here and in the following formulae we have omitted the lepton and hadron mass terms when it is not of importance for the argumentation.) Since the Jacobian  $d(y_i, Q_i^2)/d(x_i, Q_i^2) = 1$ , either variable would be an equally valid choice for covering the phase space. Small  $x_i$  values will be of less interest for us, since they lead to small  $W^2$  and hence no high- $p_\perp$  jet production, so  $y_i/x_i \approx 1$  except in the high- $Q^2$  tail, and often the two are used interchangeably. Unless special  $Q^2$  cuts are imposed, cross sections obtained with  $f_{\gamma/l}^{\text{T,L}}(x, Q^2) dx$  rather than  $f_{\gamma/l}^{\text{T,L}}(y, Q^2) dy$  differ only at the per mil level. For comparisons with experimental cuts, it is sometimes relevant to know which of the two is being used in an analysis.

In the ep kinematics, the  $x$  and  $y$  definitions give that

$$W^2 = xs = ys - Q^2. \quad (10)$$

The  $W^2$  expression for  $l^+l^-$  is more complicated, especially because of the dependence on the relative azimuthal angle of the scattered leptons,  $\varphi_{12} = \varphi_1 - \varphi_2$ :

$$\begin{aligned} W^2 &= x_1 x_2 s + \frac{2Q_1^2 Q_2^2}{s} - 2\sqrt{1 - x_1 - \frac{Q_1^2}{s}} \sqrt{1 - x_2 - \frac{Q_2^2}{s}} Q_1 Q_2 \cos \varphi_{12} \\ &= y_1 y_2 s - Q_1^2 - Q_2^2 + \frac{Q_1^2 Q_2^2}{s} - 2\sqrt{1 - y_1} \sqrt{1 - y_2} Q_1 Q_2 \cos \varphi_{12}. \end{aligned} \quad (11)$$

The lepton scattering angle  $\theta_i$  is related to  $Q_i^2$  as

$$Q_i^2 = \frac{x_i^2}{1-x_i} m_i^2 + (1-x_i) \left( s - \frac{2}{(1-x_i)^2} m_i^2 - 2m_j^2 \right) \sin^2(\theta_i/2) , \quad (12)$$

with  $m_i^2 = k_i^2 = k_i'^2$  and terms of  $O(m^4)$  neglected. The kinematical limits thus are

$$(Q_i^2)_{\min} \approx \frac{x_i^2}{1-x_i} m_i^2 , \quad (13)$$

$$(Q_i^2)_{\max} \approx (1-x_i)s , \quad (14)$$

unless experimental conditions reduce the  $\theta_i$  ranges.

In summary, we will allow the possibility of experimental cuts in the  $x_i$ ,  $y_i$ ,  $Q_i^2$ ,  $\theta_i$  and  $W^2$  variables. Within the allowed region, the phase space is Monte Carlo sampled according to  $\prod_i (dQ_i^2/Q_i^2) (dx_i/x_i) d\varphi_i$ , with the remaining flux factors combined with the cross section factors to give the event weight used for eventual acceptance or rejection.

## 2.2 Photon Processes

The hard-scattering processes are classified according to whether one or both photons are resolved. For completeness we here quote some of the less familiar cross sections.

For the direct process  $\gamma^* \gamma^* \rightarrow f\bar{f}$ ,  $f$  some fermion, the cross sections are [18]

$$\frac{d\sigma_{\text{TT}}}{d\hat{t}} = 2\pi\alpha_{\text{em}}^2 N_f e_f^4 \frac{\hat{t}\hat{u} - Q_1^2 Q_2^2}{\lambda^2 \hat{t}^2 \hat{u}^2} \{ (\hat{t}^2 + \hat{u}^2) [1 - 2F(1-F)] - 2Q_1^2 Q_2^2 F^2 \} , \quad (15)$$

$$\frac{d\sigma_{\text{TL}}}{d\hat{t}} = 8\pi\alpha_{\text{em}}^2 N_f e_f^4 \frac{Q_2^2 \hat{s}}{\lambda^4 \hat{t}^2 \hat{u}^2} \left\{ 2(\hat{t}\hat{u} - Q_1^2 Q_2^2) \left[ \hat{t}\hat{u} + \frac{Q_1^2 \hat{s}(\hat{t} - \hat{u})^2}{\lambda^2} \right] + Q_1^4 (\hat{t} - \hat{u})^2 \right\} , \quad (16)$$

$$\frac{d\sigma_{\text{LT}}}{d\hat{t}} = \frac{d\sigma_{\text{TL}}}{d\hat{t}} (Q_1^2 \leftrightarrow Q_2^2) , \quad (17)$$

$$\frac{d\sigma_{\text{LL}}}{d\hat{t}} = 32\pi\alpha_{\text{em}}^2 N_f e_f^4 \frac{Q_1^2 Q_2^2 \hat{s}^2}{\lambda^6 \hat{t}^2 \hat{u}^2} (\hat{t}\hat{u} - Q_1^2 Q_2^2) (\hat{t} - \hat{u})^2 , \quad (18)$$

with  $\hat{s} = W^2$ ,

$$\lambda = \sqrt{(\hat{s} + Q_1^2 + Q_2^2)^2 - 4Q_1^2 Q_2^2} , \quad (19)$$

$$F = \frac{\hat{s}(\hat{s} + Q_1^2 + Q_2^2)}{\lambda^2} , \quad (20)$$

$e_f$  the electrical charge and  $N_f$  the colour factor, 3 for a quark and 1 for a lepton. Remember that  $\hat{s} + \hat{t} + \hat{u} = -Q_1^2 - Q_2^2$ , neglecting the fermion mass. Note that the cross section for a longitudinal photon vanishes as  $Q_i^2$  in the limit  $Q_i^2 \rightarrow 0$ .

For a resolved photon, the photon virtuality scale is included in the arguments of the parton distribution but, in the spirit of the parton model, the virtuality of the parton inside the photon is not included in the matrix elements. Neither is the possibility of the partons being in longitudinally polarized photons (see below, however). The same subprocess cross sections can therefore be used for direct  $\gamma^* p$  processes and for single-resolved  $\gamma^* \gamma^*$  ones. For  $\gamma^* q \rightarrow gq$  one obtains [19]

$$\frac{d\hat{\sigma}_{\text{T}}}{d\hat{t}} = \frac{8}{3} \pi \alpha_s \alpha_{\text{em}} e_q^2 \frac{1}{(\hat{s} + Q_1^2)^2} \left\{ \frac{\hat{s}^2 + \hat{u}^2 - 2Q_1^2 \hat{t}}{-\hat{s}\hat{u}} - \frac{2Q_1^2 \hat{t}}{(\hat{s} + Q_1^2)^2} \right\} , \quad (21)$$

$$\frac{d\hat{\sigma}_{\text{L}}}{d\hat{t}} = \frac{8}{3} \pi \alpha_s \alpha_{\text{em}} e_q^2 \frac{-4Q_1^2 \hat{t}}{(\hat{s} + Q_1^2)^4} , \quad (22)$$

and for  $\gamma^* g \rightarrow q\bar{q}$

$$\frac{d\hat{\sigma}_T}{d\hat{t}} = \pi\alpha_s\alpha_{\text{em}}e_q^2 \frac{1}{(\hat{s} + Q_1^2)^2} \frac{\hat{t}^2 + \hat{u}^2}{\hat{t}\hat{u}} \left[ 1 - \frac{2Q_1^2\hat{s}}{(\hat{s} + Q_1^2)^2} \right], \quad (23)$$

$$\frac{d\hat{\sigma}_L}{d\hat{t}} = \pi\alpha_s\alpha_{\text{em}}e_q^2 \frac{8Q_1^2\hat{s}}{(\hat{s} + Q_1^2)^4}. \quad (24)$$

Convolution with parton distributions gives

$$d\sigma(\gamma^* p \rightarrow \mathbf{X}) = \iint d\hat{x}_2 d\hat{t} f_i^p(\hat{x}_2, \mu^2) \frac{d\hat{\sigma}}{d\hat{t}}(\hat{s} = \hat{x}_2 W^2), \quad (25)$$

$$d\sigma(\gamma^* \gamma^* \rightarrow \mathbf{X}) = \iint d\hat{x}_2 d\hat{t} f_i^{\gamma^*}(\hat{x}_2, \mu^2, Q_2^2) \frac{d\hat{\sigma}}{d\hat{t}}(\hat{s} = \hat{x}_2 W^2), \quad (26)$$

where  $\mu^2$  is the scale of the hard-scattering subprocess.

Finally we come to resolved processes in  $\gamma^* p$  and doubly-resolved ones in  $\gamma^* \gamma^*$ . There are six basic QCD cross sections,  $qq' \rightarrow qq'$ ,  $q\bar{q} \rightarrow q'\bar{q}'$ ,  $q\bar{q} \rightarrow gg$ ,  $qg \rightarrow qg$ ,  $gg \rightarrow gg$  and  $gg \rightarrow q\bar{q}$ . Since again parton virtualities are not included, these are the expressions familiar from pp physics [20] and are not listed here. Again a convolution with parton distributions is necessary,

$$d\sigma(\gamma^* p \rightarrow \mathbf{X}) = \iiint d\hat{x}_1 d\hat{x}_2 d\hat{t} f_i^{\gamma^*}(\hat{x}_1, \mu^2, Q_1^2) f_j^p(\hat{x}_2, \mu^2) \frac{d\hat{\sigma}}{d\hat{t}}(\hat{s} = \hat{x}_1 \hat{x}_2 W^2), \quad (27)$$

$$d\sigma(\gamma^* \gamma^* \rightarrow \mathbf{X}) = \iiint d\hat{x}_1 d\hat{x}_2 d\hat{t} f_i^{\gamma^*}(\hat{x}_1, \mu^2, Q_1^2) f_j^{\gamma^*}(\hat{x}_2, \mu^2, Q_2^2) \frac{d\hat{\sigma}}{d\hat{t}}(\hat{s} = \hat{x}_1 \hat{x}_2 W^2). \quad (28)$$

In line with the neglect of parton masses, also the  $\hat{s}$  expression for  $\gamma^* \gamma^*$  is simpler than its  $W^2$  analogue in eq. (11). When initial-state radiation is subsequently included, both transverse momenta and spacelike parton virtualities are generated, but in such a way that the relation  $\hat{s} = \hat{x}_1 \hat{x}_2 W^2$  is maintained [21]. Differences between alternative  $\hat{s}$  definitions being subleading, they are beyond our standard QCD accuracy.

## 2.3 Parton Distributions

One major element of model dependence enters via the choice of parton distributions for a resolved virtual photon. These distributions contain a hadronic component that is not perturbatively calculable. It is therefore necessary to parameterize the solution with input from experimental data, which mainly is available for (almost) real photons. In the following we will use the SaS distributions [3], which are the ones best suited for our formalism. Another set of distributions is provided by GRS [22], while a simpler recipe for suppression factors relative to real photons has been proposed by DG [23].

The SaS distributions for a real photon can be written as

$$f_a^\gamma(x, \mu^2) = \sum_V \frac{4\pi\alpha_{\text{em}}}{f_V^2} f_a^{\gamma,V}(x, \mu^2; Q_0^2) + \frac{\alpha_{\text{em}}}{2\pi} \sum_q 2e_q^2 \int_{Q_0^2}^{\mu^2} \frac{dk^2}{k^2} f_a^{\gamma,q\bar{q}}(x, \mu^2; k^2). \quad (29)$$

Here the sum is over a set of vector mesons  $V = \rho^0, \omega, \phi, J/\psi$  according to a vector-meson-dominance ansatz for low-virtuality fluctuations of the photon, with experimentally determined couplings  $4\pi\alpha_{\text{em}}/f_V^2$ . The higher-virtuality, perturbative, fluctuations are

represented by an integral over the virtuality  $k^2$  and a sum over quark species. We will refer to the first part as the VMD one and the second as the anomalous one. Each component  $f^{\gamma,V}$  and  $f^{\gamma,q\bar{q}}$  obeys a unit momentum sum rule, and also obeys normal QCD evolution equations. The  $f^{\gamma,V}(x, Q_0^2)$  have to be determined by a tune to  $F_2^\gamma(x, \mu^2)$  data, while  $f^{\gamma,q\bar{q}}$  evolve from the boundary condition

$$f_a^{\gamma,q\bar{q}}(x, k^2; k^2) = \frac{3}{2} (x^2 + (1-x)^2) (\delta_{aq} + \delta_{a\bar{q}}) . \quad (30)$$

The  $\mu^2$  dependence enter both via the evolution of each component and via the upper limit of the  $dk^2$  integral. It is the latter dependence that generates the so-called anomalous term of the photon distribution evolution equations, from which the terminology has been taken over for the related event class.

From the above ansatz, the extension to a virtual photon is given by the introduction of a dipole dampening factor for each component,

$$\begin{aligned} f_a^{\gamma*}(x, \mu^2, Q^2) &= \sum_V \frac{4\pi\alpha_{\text{em}}}{f_V^2} \left( \frac{m_V^2}{m_V^2 + Q^2} \right)^2 f_a^{\gamma,V}(x, \mu^2; \tilde{Q}_0^2) \\ &+ \frac{\alpha_{\text{em}}}{2\pi} \sum_q 2e_q^2 \int_{Q_0^2}^{\mu^2} \frac{dk^2}{k^2} \left( \frac{k^2}{k^2 + Q^2} \right)^2 f_a^{\gamma,q\bar{q}}(x, \mu^2; k^2) . \end{aligned} \quad (31)$$

Thus, with increasing  $Q^2$ , the VMD components die away faster than the anomalous ones, and within the latter the low- $k^2$  ones faster than the high- $k^2$  ones. In the VMD component, the effective evolution range is reduced by the introduction of a  $\tilde{Q}_0^2 = Q_{\text{int}}^2 = Q_0 Q_{\text{eff}} > Q_0^2$ , with

$$Q_{\text{eff}}^2 = \mu^2 \frac{Q_0^2 + Q^2}{\mu^2 + Q^2} \exp \left\{ \frac{Q^2(\mu^2 - Q_0^2)}{(\mu^2 + Q^2)(Q_0^2 + Q^2)} \right\} . \quad (32)$$

As a technical trick, the handling of the  $k^2$  integral is made more tractable by replacing the dipole factor by a  $k^2$ -independent multiplicative factor and an increased lower limit  $Q_{\text{int}}^2$  of the integral, in such a way that both the momentum sum and the average evolution range is unchanged. Finally, correction factors are introduced to ensure that  $f_a^{\gamma*}(x, \mu^2, Q^2) \rightarrow 0$  for  $\mu^2 \rightarrow Q^2$ : in the region  $Q^2 > \mu^2$  a fixed-order perturbative description is more appropriate than the leading-log description in terms of a resolved photon. We then arrive at the so-called modified  $P_{\text{int}}$  scheme, which is the one used here.

Since the probed real photon is purely transverse, the above ansatz does not address the issue of parton distributions of the longitudinal virtual photons. One could imagine an ansatz based on longitudinally polarized vector mesons, and branchings  $\gamma_L^* \rightarrow q\bar{q}$ , but currently no parameterization exists along these lines. We will therefore content ourselves by exploring alternatives based on applying simple multiplicative factors  $R$  to the results obtained for a resolved transverse photon. As usual, processes involving longitudinal photons should vanish in the limit  $Q^2 \rightarrow 0$ . To study two extremes, the region with a linear rise in  $Q^2$  is defined either by  $Q^2 < \mu^2$  or by  $Q^2 < m_\rho^2$ , where the former represents the perturbative and the latter some non-perturbative scale. Also the high- $Q^2$  limit is not well constrained; we will compare two different alternatives, one with an asymptotic fall-off like  $1/Q^2$  and another which approaches a constant ratio, both with respect to the transverse resolved photon. (Since we put  $f_a^{\gamma*}(x, \mu^2, Q^2) = 0$  for  $Q^2 > \mu^2$ , the  $R$  value



will actually not be used for large  $Q^2$ , so the choice is not so crucial.) We therefore study the alternative ansätze

$$R_1(y, Q^2, \mu^2) = 1 + a \frac{4\mu^2 Q^2}{(\mu^2 + Q^2)^2} \frac{f_{\gamma/l}^L(y, Q^2)}{f_{\gamma/l}^T(y, Q^2)}, \quad (33)$$

$$R_2(y, Q^2, \mu^2) = 1 + a \frac{4Q^2}{(\mu^2 + Q^2)} \frac{f_{\gamma/l}^L(y, Q^2)}{f_{\gamma/l}^T(y, Q^2)}, \quad (34)$$

$$R_3(y, Q^2, \mu^2) = 1 + a \frac{4Q^2}{(m_\rho^2 + Q^2)} \frac{f_{\gamma/l}^L(y, Q^2)}{f_{\gamma/l}^T(y, Q^2)} \quad (35)$$

with  $a = 1$  as main contrast to the default  $a = 0$ . The  $y$  dependence compensates for the difference in photon flux between transverse and longitudinal photons.  $R_1$  and  $R_2$  have the same onset at low  $Q^2$  but different asymptotic behaviour; for the former case the longitudinal part vanishes and for the latter it approaches a constant (w.r.t. the transverse case). For the third case the onset is governed by a non-perturbative parameter  $m_\rho$  and it has the same asymptotic limit as  $R_2$ . In a more sophisticated treatment, presumably also the  $k^2$  scale of the  $\gamma^* \rightarrow q\bar{q}$  fluctuation would enter. In double-resolved  $\gamma^*\gamma^*$  events one  $R$  factor is applied for each side.

Another ambiguity is the choice of  $\mu^2$  scale in parton distributions. For a process such as  $\gamma\gamma \rightarrow q\bar{q}$ , with real photons, conventional wisdom is that  $\mu^2 = -\hat{t}$  is the proper scale in the limit  $\hat{t} \rightarrow 0$ , where  $t$ -channel graphs dominate the cross sections, and  $\mu^2 = -\hat{u}$  in the limit  $\hat{u} \rightarrow 0$ . The combination  $\mu^2 = \hat{t}\hat{u}/\hat{s} = p_\perp^2$  interpolates between these limits and thus is a traditional choice, sometimes multiplied by some constant factor. When the incoming (or outgoing) photons/partons are not massless,  $\hat{t}\hat{u}/\hat{s} \neq p_\perp^2$ . A possible generalization for a direct virtual photon,  $Q_1^2 \neq 0$ , is

$$\mu^2 = -\frac{\hat{t}\hat{u}}{\hat{t} + \hat{u}} = \frac{\hat{t}\hat{u}}{\hat{s} + Q_1^2} = p_\perp^2 \frac{\hat{s} + Q_1^2}{\hat{s}}. \quad (36)$$

For a corresponding  $t$ -channel graph involving the quark from a resolved photon, in principle the same relation should hold, with the quark virtuality  $\hat{Q}_1^2$  substituting for the photon  $Q_1^2$  one. Inside PYTHIA, however, all incoming partons are assumed massless in the selection of hard-scattering kinematics. When, later on, the  $\gamma^* \rightarrow q\bar{q}$  branching is included, the  $\hat{s}$  and the rest-frame scattering angle are left unaffected. Thus also  $p_\perp^2$  is unchanged, while  $\hat{t}$  and  $\hat{u}$  are not. Using the corrected values, one obtains the same final expression as in eq. (36), with  $\hat{Q}_1^2$  instead of  $Q_1^2$ . Kinematics provides the constraint  $\hat{Q}_1^2 > x_1 Q_1^2$  at the  $\gamma^* \rightarrow q\bar{q}$  branching. The lower bound is a rather conservative estimate of the actual value of  $\hat{Q}_1^2$ , however, and more typically one obtains  $\hat{Q}_1^2 \approx Q_1^2$  from the  $\gamma^* \rightarrow q\bar{q}$  branching. (Further branchings are included in the standard QCD parton-shower description. By analogy with the description of other QCD processes, we here disregard these shower virtualities.) A scale choice like in eq. (36) therefore should be a sensible one both for direct and resolved photons.

When both incoming photons are virtual, the relation between  $\mu^2$  and  $p_\perp^2$  becomes more complicated, but in the limit that terms of order  $Q_1^2 Q_2^2 / \hat{s}^2$  are neglected, they simplify to

$$\mu^2 = p_\perp^2 \frac{\hat{s} + Q_1^2 + Q_2^2}{\hat{s}}. \quad (37)$$

This expression does not guarantee that  $\mu^2 > Q_1^2 + Q_2^2$ . Sometimes such an inequality is assumed [24], so in order to cover a broader range of scale choices, below we will be comparing six different alternatives. In (almost) increasing order these are

$$\mu_1^2 = p_\perp^2, \quad (38)$$

$$\mu_2^2 = p_\perp^2 \frac{\hat{s} + x_1 Q_1^2 + x_2 Q_2^2}{\hat{s}}, \quad (39)$$

$$\mu_3^2 = p_\perp^2 \frac{\hat{s} + Q_1^2 + Q_2^2}{\hat{s}}, \quad (40)$$

$$\mu_4^2 = p_\perp^2 + \frac{Q_1^2 + Q_2^2}{2}, \quad (41)$$

$$\mu_5^2 = p_\perp^2 + Q_1^2 + Q_2^2, \quad (42)$$

$$\mu_6^2 = 2\mu_3^2. \quad (43)$$

Only the fifth alternative ensures  $f_a^{\gamma^*}(x, \mu^2, Q^2) > 0$  for arbitrarily large  $Q^2$ ; in all other alternatives the resolved contribution (at fixed  $p_\perp$ ) vanish above some  $Q^2$  scale. The last alternative exploits the well-known freedom of including some multiplicative factor in any (leading-order) scale choice. When nothing is mentioned explicitly below, the choice  $\mu_3^2$  is used. We should note that the expressions in the program also contain a dependence on final-state masses, e.g. for the production of massive quarks, but this is left out here since it is not a topic studied in this paper. (It will enter briefly in the following, however.)

## 2.4 Other Model Aspects

The issues discussed above are the main ones that distinguish the description of processes involving virtual photons from those induced by real photons or by hadrons in general. In common for the tree is the need to consider the buildup of more complicated partonic configurations from the lowest-order ‘skeletons’ defined above, (*i*) by parton showers, (*ii*) by multiple parton–parton interactions and beam remnants, where applicable, and (*iii*) by the subsequent transformation of these partons into the observable hadrons. The latter, hadronization stage can be described by the standard string fragmentation framework [25], followed by the decays of unstable primary hadrons, and is not further discussed here. In the following we comment on the shower, multiple-interaction and beam-remnant aspects.

The parton-shower description is conveniently subdivided into initial- and final-state radiation. For wide-angle emissions such a classification is not unambiguous, and it is necessary to consider interference effects in order to describe the data [26]. A direct photon is not associated with any initial-state QCD radiation.

In the hadronic environment, initial-state radiation normally means an evolution of a spacelike branch of partons, from an initially vanishing virtuality up to the scale of the hard process. The ‘backwards evolution’ strategy [21] allows this cascade to be reconstructed in reverse order. That is, from a parton  $b$  coming in to the hard scattering, the branching  $a \rightarrow bc$  that produced  $b$  is first reconstructed, thereafter the branching that produced  $a$ , and so on, down to the lower cutoff scale  $Q_0^{\text{sh}}$ , in practice of the order of 1 GeV. Inclusively, the effect of parton-shower histories is already taken into account by the  $\mu^2$  dependence of the parton distributions used to select the hard scattering, so what this procedure does is to associate an exclusive set of initial-state-radiation partons to each hard scattering.

For a real photon, the VMD part is assumed to behave like a hadron, while the lower parton-shower cut-off  $Q_0^{\text{sh}}$  has to be considered further for the anomalous component. In

the spirit of the ansatz for parton distributions, eq. (29), the  $k^2$  value of the  $\gamma \rightarrow q\bar{q}$  branching is distributed like  $dk^2/k^2$ . In principle, for a given physical process, there would be a further ‘trigger bias’ effect to this distribution: at large (small)  $x$  values a large (small)  $k^2$  would be favoured since it would be associated with a small (large) evolution range. As a first approximation, this bias is neglected here, i.e.  $k^2$  is picked flat in a logarithmic scale between  $Q_0^2$  and  $\mu^2$ . When this  $k$  is larger than the default value of  $Q_0^{\text{sh}}$ , the shower cut-off is increased to instead be given by  $k$ . Thus there is no shower evolution below the  $k$  scale of the  $\gamma \rightarrow q\bar{q}$  branching. Thereby the amount of collinear emission along the incoming photon direction is reduced for high-virtuality fluctuations.

As a technical aside, we note that the default value  $Q_0 = 0.6$  GeV is smaller than  $Q_0^{\text{sh}} = 1$  GeV. First, it should be made clear that  $k^2$  and the  $Q^2$  virtuality variable of the spacelike shower evolution are not defined in precisely the same way and therefore very well can differ by factors of order unity, so that also the lower cut-offs may differ. However, also disregarding this, there is no reason why the two cut-offs should agree. Whereas  $Q_0$  is severely constrained e.g. by  $F_2^\gamma$  data,  $Q_0^{\text{sh}}$  is just a crude estimate of where emitted partons in the cascade are so collinear that their effect may be safely neglected. That is, we do not exclude the possibility of parton emissions in the range between  $Q_0$  and  $Q_0^{\text{sh}}$ , but also do not believe that their inclusion or not is essential for a description of final-state properties. The effects of an increased shower cut-off only show up for  $\gamma \rightarrow q\bar{q}$  branchings with  $k \gtrsim 2$  GeV, in terms of a reduced parton emission rate along the incoming photon direction.

The generalization to a virtual photon is now straightforward, given the extension of  $f_a^\gamma$  to  $f_a^{\gamma^*}$ , cf. eqs. (29) and (31). For the VMD piece, the shower cut-off is selected to be the larger of  $Q_{\text{int}}$  and  $Q_0^{\text{sh}}$ . For the anomalous piece, a  $k^2$  is picked flat in a logarithmic scale between  $Q_{\text{int}}^2$  and  $\mu^2$ , and the shower cut-off is the larger of this  $k$  and  $Q_0^{\text{sh}}$ .

Final-state radiation from the scattered partons of the hard interaction follow the same pattern as in hadron–hadron collisions, and so need not be discussed here. Also time-like partons on the ‘side branches’ of an initial-state cascade can undergo final-state evolution, as part of the conventional shower description. The new aspect concerns the  $\bar{q}$  ‘beam remnant’ parton of an anomalous  $\gamma^* \rightarrow q\bar{q}$  branching, where the  $q$  is the initiator of the spacelike cascade. This parton can undergo a shower evolution from the  $\gamma^* \rightarrow q\bar{q}$  branching scale  $k$  down to the timelike shower cut-off  $m_0^{\text{sh}} \approx 1$  GeV, provided  $k$  is above the cut-off. For the VMD part of the photon, the beam remnant is assumed not to radiate.

In general, a beam remnant contains the flavours ‘left behind’ when one parton initiates the spacelike shower that leads up to the hard interaction. Momentum conservation gives its kinematics. This includes both a longitudinal momentum fraction  $1 - x$ , if the initiator takes  $x$ , and a transverse ‘primordial  $k_\perp$ ’ recoil. For the VMD components of the photon this transverse momentum should be of a nonperturbative character and small,  $\sim 0.5$  GeV, although there are indications of much larger values in data [27]. A Gaussian ansatz is used to pick a  $k_\perp$  vector. For the anomalous part of the photon, we associate its  $k_\perp$  with the  $k$  scale that already figured prominently above.

Multiple parton–parton interactions [28, 2] could be viewed as a further sophistication of the beam-remnant description. The basic idea is that hadronic states contain many partons and that therefore several perturbative interactions may occur in a hadron–hadron collision. Usually (at most) one of these give rise to visible high- $p_\perp$  jets, while the rest only add to the underlying event activity. This additional component is vitally needed in order to reproduce the observed multiplicity and  $E_\perp$  flow in high-energy  $p\bar{p}$  collisions, at least if string hadronization is supposed to be universal, i.e. have its parameters constrained by

$e^+e^-$  data. The main unknown parameter in this approach is  $p_{\perp,\min}^{\text{MI}} \approx 2$  GeV, the scale below which perturbation theory is assumed not to be applied anymore. Physically, this scale can be viewed as related to an effective colour screening phenomenon: gluons with a wavelength larger than  $1/p_{\perp,\min}^{\text{MI}}$  do not resolve the colour structure inside the hadron wave function and therefore decouple. Of course, this screening should set in gradually, so  $p_{\perp,\min}^{\text{MI}}$  is only an effective parameter. To first approximation, the average number of interactions per event is the ratio of the jet cross section above  $p_{\perp,\min}^{\text{MI}}$  to the total inelastic cross section. By now there exist convincing evidence in favour of multiple interactions also in the HERA data [29].

Almost by definition, direct and single-resolved processes do not lead to multiple interactions. Furthermore, within the spectrum of resolved components of a real photon, one would expect a close-to hadronlike behaviour for the VMD part and then a gradual fading-away of multiple interactions as the  $k^2$  scale of an anomalous fluctuation is increased. This may partly be seen as a consequence of that the number of partons (above some fixed  $x_0$ ) decrease with increasing  $k^2$ . Furthermore, the physical size of an anomalous fluctuation should scale like  $1/k$ , so the screening argument above would lead to a scaling-up of  $p_{\perp,\min}^{\text{MI}}$  roughly by a factor  $k/Q_0$ . This in part would be compensated by an expected decrease in the total cross section of an anomalous fluctuation, about like  $1/k^2$  based on the size scaling argument, but in total there should still be a rather rapid fall-off with  $k$ . As a first approximation, we follow the route adopted in [2], namely to allow multiple interactions for VMD states to the same extent as for hadrons, and not at all for the anomalous states.

When generalizing to virtual photons, the same arguments as used above for the anomalous component would suggest a fall-off of multiple interactions in the VMD component with increasing  $Q^2$  scale. As a first guess, we have here chosen to scale up  $p_{\perp,\min}^{\text{MI}}$  like  $\sqrt{1 + Q^2/m_V^2}$ , while the normalizing total cross section is scaled down like  $m_V^4/(m_V^2 + Q^2)^2$  in accordance with the dipole ansatz.

## 3 Results

### 3.1 Basic Distributions

#### 3.1.1 $\gamma^*p$ Partonic Cross Sections

The contribution to the  $\sigma_{\gamma^*p}$  parton cross section from the different direct components in equations (21)–(24), the boson–gluon fusion and the QCD Compton processes, are shown in Fig. 2 as a function of the photon virtuality,  $Q^2$ . The partons produced in the  $2 \rightarrow 2$  hard scattering subprocess are restricted to have transverse momenta  $p_{\perp}$  larger than 5 GeV and the hadronic centre of mass energy  $W = \sqrt{s_{\gamma^*p}}$  is equal to 200 GeV.

In the limit  $Q^2 \rightarrow 0$  the cross section vanishes for the processes involving a longitudinal photon. In the same limit the boson–gluon fusion process with a transverse photon,  $\gamma_T^*g \rightarrow q\bar{q}$ , is more important than the QCD Compton counterpart,  $\gamma_T^*q \rightarrow gq$ ; this kinematic region permits the gluon/quark from the proton to have a small fraction  $x$  of the proton momentum,  $x = (\hat{s} + Q^2)/(W^2 + Q^2)$ . At large  $Q^2$ , the opposite is true;  $x$  is large and the QCD Compton process, involving an initial quark from the proton, is more important than the boson–gluon fusion process. Both processes are suppressed by the  $1/(\hat{s} + Q^2)^2$  factor that provides the main dampening at large  $Q^2$ . The longitudinal

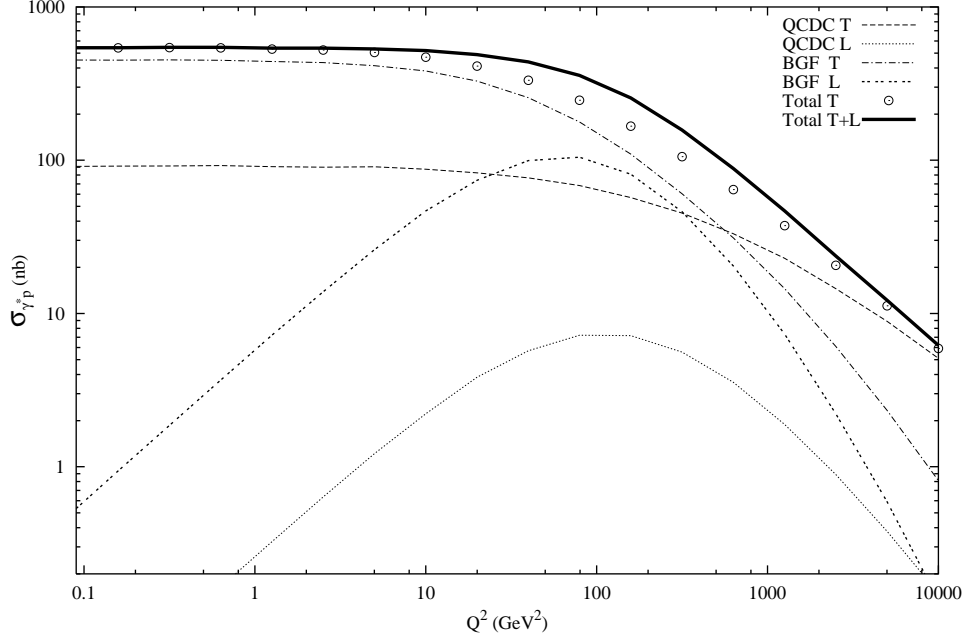


Figure 2: Contributions to the  $\sigma_{\gamma^*p}$  parton cross section from the subprocesses in equations (21)–(24),  $p_{\perp}^{\text{parton}} > 5$  GeV and  $W_{\gamma^*p} = 200$  GeV. The circles and the solid line is the sum of the transverse (T) and the transverse plus the longitudinal (T+L) direct processes respectively.

processes,  $\gamma_L^*q \rightarrow gq$  and  $\gamma_L^*g \rightarrow q\bar{q}$  have maximal cross sections when  $Q^2 \sim \hat{s}$ , since  $\hat{s} \geq 4p_{\perp,\text{min}}$  this occurs for  $Q^2$  around 100 GeV<sup>2</sup>.

The proton structure function used to produce Fig. 2 was GRV 94 LO, which is the default in PYTHIA. A different choice of structure function would only change the details but not the conclusions made from these results. In the following the GRV 94 LO will be used as the proton parton distribution except where otherwise stated.

When studying jet production with low photon virtualities it is likely that the photon is resolved. The photon fluctuates then into a quark-antiquark pair that develops into a multiparton state and finally one of these partons scatters off a parton from the proton. The virtual photon parton distributions used for modeling the resolved components are the SaS 1D and 2D distributions. The dipole factors in eq. (31) will dampen the resolved components with increasing photon virtualities.

The relative importance of the direct components compared to the resolved components — the VMD and anomalous fluctuations — are shown in Fig. 3. The direct contribution is the sum of the transverse QCD Compton and boson–gluon fusion processes studied in Fig. 2. As expected, the VMD components die away faster than the anomalous ones which in turn die away faster than the sum of the direct components. Here we also see the difference between the SaS 1D and SaS 2D distributions, with SaS 2D having a higher cut-off for the separation between the VMD component and the anomalous component. This is reflected by the larger contribution from the SaS 2D VMD component compared to the SaS 1D one, and vice versa for the anomalous component.

Longitudinal resolved components are simulated with an extra factor of  $R_1(y, Q^2, \mu^2)$ , eq. (33), for the transverse resolved components. In Fig. 3 an  $a$ -parameter equal to 1

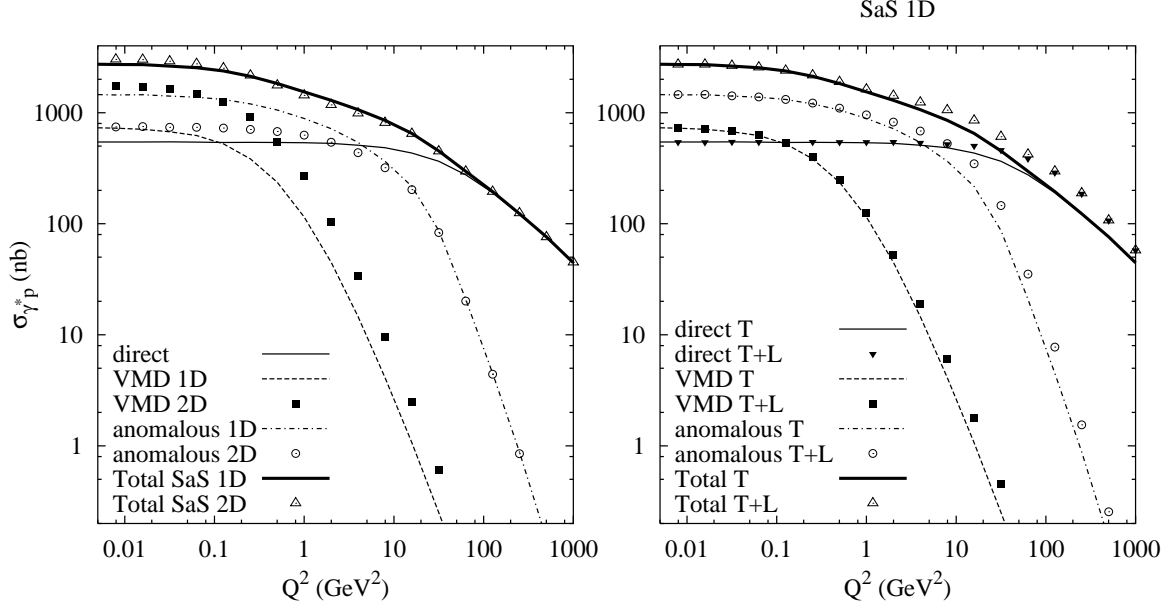


Figure 3: Contributions to the  $\sigma_{\gamma^*p}$  parton cross section from events involving a direct, a VMD and an anomalous photon,  $p_{\perp}^{\text{parton}} > 5$  GeV and  $\sqrt{s_{\gamma^*p}} = 200$  GeV. To the left, the SaS 1D and SaS 2D parton distributions was used, to the right SaS 1D was used and a longitudinal resolved photon is modeled with  $a = 1$  and  $y = 0.44$  (see text).

has been used together with the SaS 1D photon parton distribution. The  $y$  value is set equal to 0.44 with HERA energies in mind. A noticeable difference is seen in the total jet cross section for  $Q^2$  around 10 GeV<sup>2</sup>, since, in this ansatz, the maximal contribution for the longitudinal component is obtained at  $Q^2 = \mu^2$ , and the direct and the anomalous component is of the same order in this region. With  $a = 1$  the sum of the resolved components can be almost a factor of two larger than with  $a = 0$ , the case with pure transverse resolved photons. There is nothing special with the choice  $a = 1$  except that it models a longitudinal resolved component that is of the same order of magnitude as the transverse component at intermediate  $Q^2$  values; this is the same behaviour as seen for the direct components.

### 3.1.2 $\gamma^*\gamma^*$ Partonic Cross Sections

In Fig. 4 the processes  $\gamma_{T,L}^*\gamma_{T,L}^* \rightarrow q\bar{q}$ , equations (15)–(18), have been generated at a centre of mass energy  $W = \sqrt{s_{\gamma^*\gamma^*}}$  of 100 GeV. For simplicity, one of the photons was kept at a fixed virtuality of 0.1 GeV<sup>2</sup> or 10 GeV<sup>2</sup>, respectively. The transverse momenta for the partons in the hard scattering was restricted to be larger than 5 GeV.

Clearly, the dominant process is  $\gamma_T^*\gamma_T^* \rightarrow q\bar{q}$  but, as the virtuality  $Q_1^2$  increases, the contribution from the longitudinal processes becomes more and more important. From eq. (15)–(18) we notice that the  $\gamma_T^*\gamma_L^*$ ,  $\gamma_L^*\gamma_T^*$  and  $\gamma_L^*\gamma_L^*$  direct cross sections have a maximum at  $Q_1^2 \sim \hat{s} = s_{\gamma^*\gamma^*}$  (for  $Q_2^2 \ll \hat{s}$ ). The  $\gamma_L^*\gamma_L^*$  process is bounded to never be larger than twice the  $\gamma_T^*\gamma_L^*$  or  $\gamma_L^*\gamma_T^*$  process. The  $\gamma_L^*\gamma_T^*$  and  $\gamma_L^*\gamma_L^*$  processes clearly go to zero as  $Q_1^2 \rightarrow 0$ , the  $\gamma_T^*\gamma_L^*$  process remains finite and approaches the expression for the  $\gamma_L^*g$  matrix element, eq. (24), with appropriate factors exchanged (and  $Q_2^2 \rightarrow Q_1^2$ ). The  $Q_2^2$  proportionality for

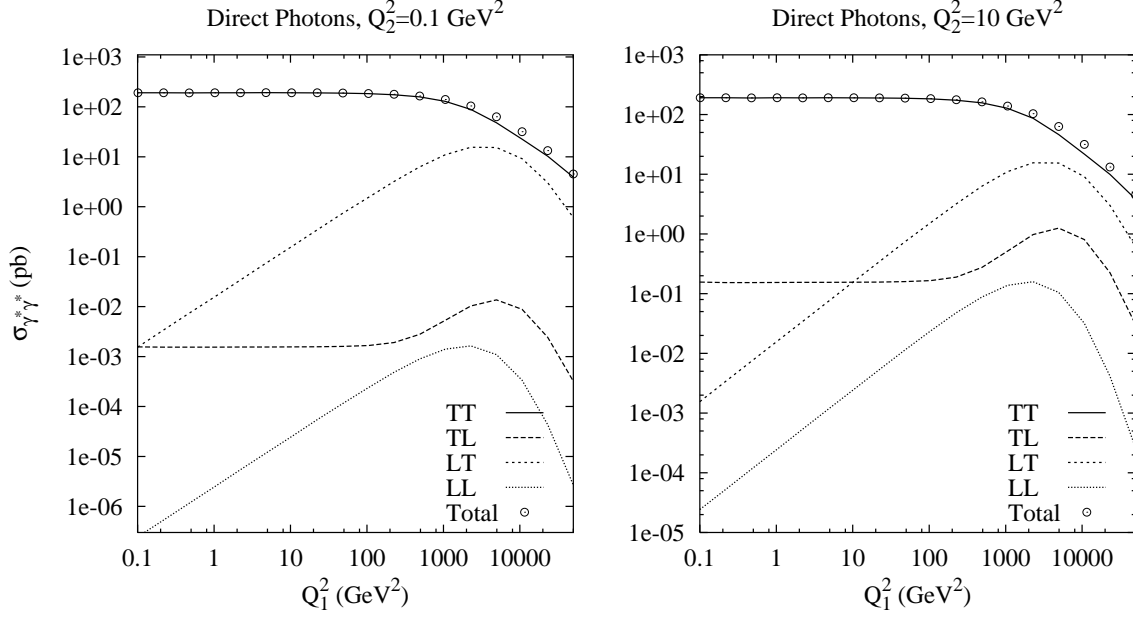


Figure 4: Contributions to the  $\sigma_{\gamma^*\gamma^*}$  parton cross section from the subprocesses in equations (15)–(18),  $p_{\perp}^{\text{parton}} > 5$  GeV and  $\sqrt{s_{\gamma^*\gamma^*}} = 100$  GeV. The  $Q_1^2$  of the first photon is varied while the second photon is kept at the fixed virtualities  $Q_2^2 = 0.1$  GeV<sup>2</sup> or  $Q_2^2 = 10$  GeV<sup>2</sup>, respectively.

the  $\gamma_T^*\gamma_L^*$  and  $\gamma_L^*\gamma_L^*$  matrix elements gives the factor of 100 difference between the two cases in Fig. 4. As for the case with direct processes in  $\gamma^*p$ , the  $\gamma_{\xi_1}^*\gamma_{\xi_2}^* \rightarrow q\bar{q}$  processes ( $\xi_i = T, L$ ) are suppressed by the  $1/\lambda^2$  factor for high  $Q_i^2$ .

With the possibility of having resolved photons, nine event classes is obtained. They are illustrated in Fig. 5 for the SaS 1D and SaS 2D parton distributions, with the second photon having the fixed virtuality  $Q_2^2 = 1$  GeV<sup>2</sup>. Generally, as  $Q_1^2$  increases, the VMD components (of the first photon) drops first, then the anomalous components and at very high  $Q_1^2$  remains the direct components (direct–direct, direct–VMD and direct–anomalous). Particularly, with the choice  $Q_2^2 = 1$  GeV<sup>2</sup>, the anomalous–anomalous events dominates at low  $Q_1^2$  for the SaS 1D case, whereas for the SaS 2D case, the VMD components dominate. In this ansatz, the  $Q_{\text{int}}$  scheme, the parton distribution for the anomalous component  $f_a^{\gamma^*}(x, \mu^2, Q^2) = 0$  when  $\mu^2 < Q^2$ .

With the  $y$ -values taken equal to 0.5 ( $s_{\gamma^*\gamma^*} \simeq y_1 y_2 s_{e^+e^-}$ ,  $\sqrt{s_{e^+e^-}} \simeq 200$  GeV) and  $a = 1$  for  $R_1(y, Q^2, \mu^2)$ , the longitudinally resolved photon contribution can be obtained as the difference between the *Total T+L* and the *Total T* in Fig. 5. Again, we see that the contribution is most pronounced where  $p_{\perp, \text{min}}^2 \simeq Q^2$ . For this special case, it happens to be where the anomalous component (of the first photon) is comparable with the direct one.

### 3.1.3 $x_{\gamma}$ Distributions

In ep collisions the variable  $x_{\gamma}^{\text{obs}}$  is defined as [1]

$$x_{\gamma}^{\text{obs}} = \frac{E_{\perp,1}e^{-\eta_1} + E_{\perp,2}e^{-\eta_2}}{2E_{\gamma}} \quad (44)$$

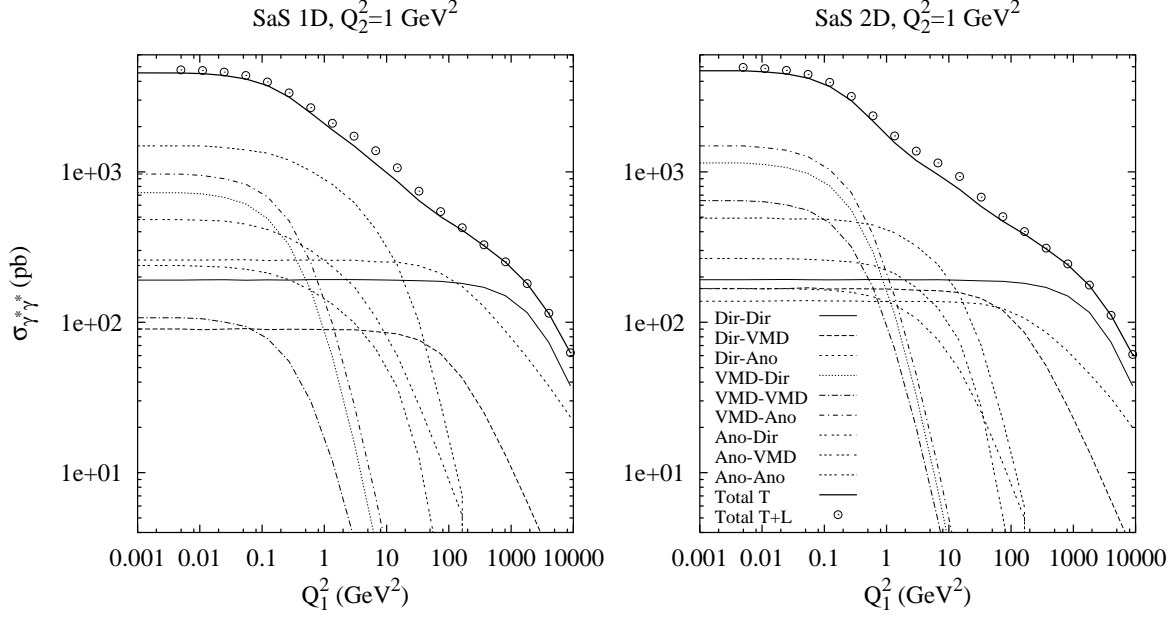


Figure 5: Contributions to the  $\sigma_{\gamma^*\gamma^*}$  parton cross section from the nine different event classes,  $p_{\perp}^{\text{parton}} > 5$  GeV and  $\sqrt{s_{\gamma^*\gamma^*}} = 100$  GeV. The  $Q_1^2$  variation is for the first photon; the second photon is kept at fixed virtuality  $Q_2^2 = 1$  GeV<sup>2</sup>.

where  $E_{\perp,i}$  is the transverse energy and  $\eta_i$  is the rapidity of the two jets with the highest transverse energy.  $E_\gamma$  is the energy of the photon.  $x_\gamma^{\text{obs}}$  is then the fraction of the photon energy (or better, light-cone momentum) that goes into the production of the two highest transverse energy jets. In Fig. 6 the  $x_\gamma^{\text{obs}}$  distribution is shown for the different photon components. A cone jet algorithm with cone radius  $R = 1$  is used for jet finding. The partons in the hard scattering are restricted to have transverse momenta larger than 3 GeV and the jets to have a transverse energy larger than 6 GeV. Note that  $p_{\perp,\text{min}}^{\text{parton}} < p_{\perp,\text{min}}^{\text{jet}}$  has been used since migration from  $p_{\perp} < p_{\perp,\text{min}}^{\text{jet}}$  is likely to happen due to various effects; this is discussed further in section 3.2. The  $x_\gamma^{\text{obs}}$  distribution was generated for two different  $Q^2$  intervals; 0.9–1.1 GeV<sup>2</sup> and 9–11 GeV<sup>2</sup>. In both cases, an  $x_\gamma^{\text{obs}}$  value of 0.7–0.8 will separate most of the direct events from the resolved events. In the low- $Q^2$  case, the SaS 2D parton distribution gives less resolved events at large  $x_\gamma^{\text{obs}}$  as compared to SaS 1D. This is because the VMD component, which is more important in SaS 2D, is dampened faster with increasing  $Q^2$  than the anomalous one. For the high- $Q^2$  case, this difference is not there, since the two anomalous components are approaching each other at high  $Q^2$ , and the VMD pieces are vanishingly small.

In  $e^+e^-$  collisions the variables  $x_\gamma^+$  and  $x_\gamma^-$  are defined as [30]

$$x_\gamma^\pm = \frac{\sum_{\text{jets}} (E \pm p_z)}{\sum_{\text{particles}} (E \pm p_z)} \quad (45)$$

where  $p_z$  is the momentum component along the  $z$ -axis of the  $e^+e^-$  collision and  $E$  is the energy of the jets or particles. The sum over jets runs over all jets in the event but is limited to the two hardest jets for dijet studies. The different direct and resolved components are shown in Fig. 7 for  $Q_i^2 < 0.8$  GeV<sup>2</sup>; each combination of components will not be shown here. For these symmetric cuts the  $x_\gamma^\pm$  distributions are identical, the



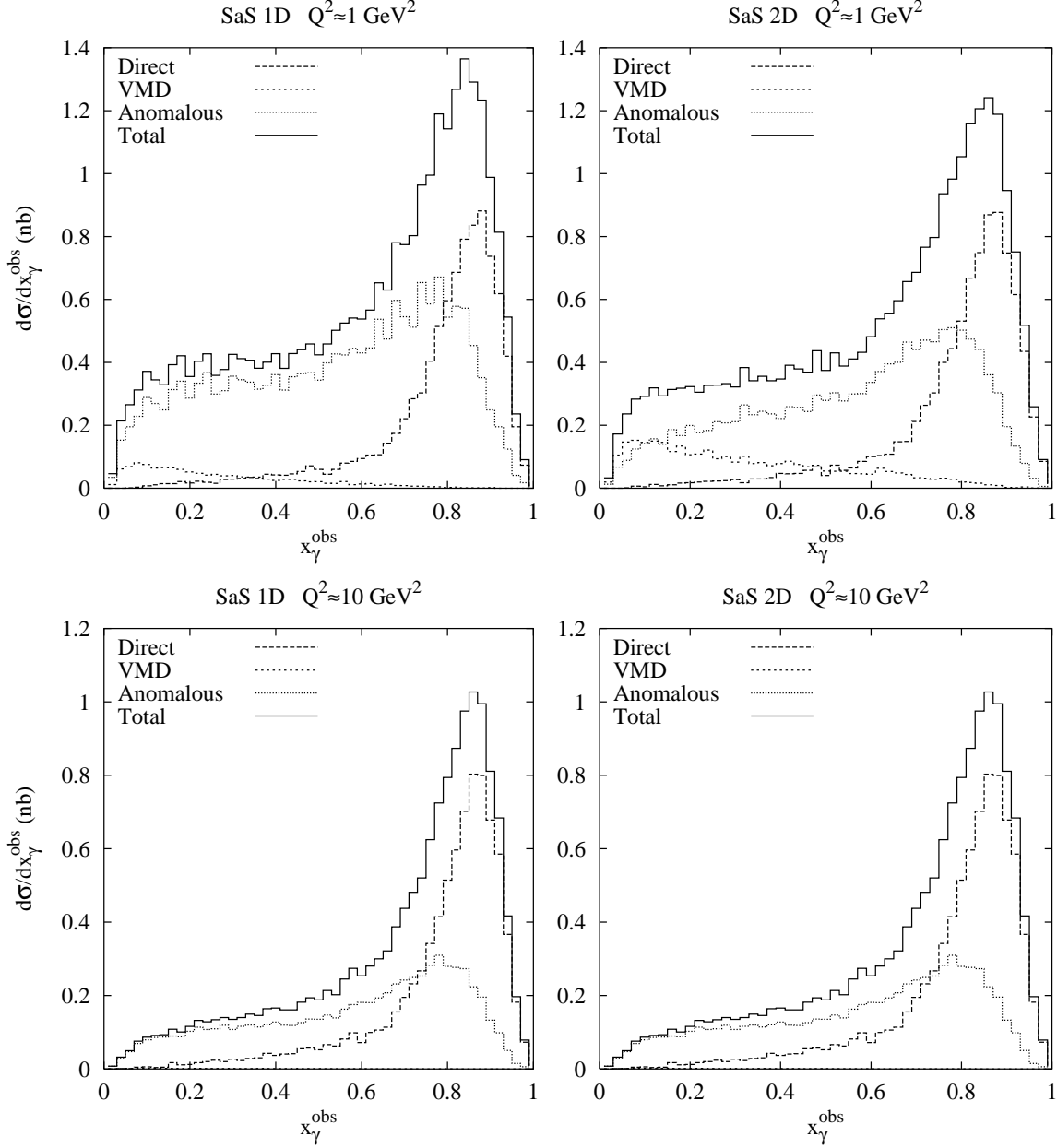


Figure 6: The  $x_\gamma^{\text{obs}}$  distribution for the different photon components.  $p_\perp^{\text{parton}} > 3 \text{ GeV}$ ,  $E_\perp^{\text{jet}} > 6 \text{ GeV}$ ,  $0.01 < y < 0.99$  and  $\sqrt{s_{\text{ep}}} \simeq 300 \text{ GeV}$ .

direct-resolved events for one case corresponds to the resolved-direct for the other. As expected, direct events are concentrated at large  $x_\gamma^\pm$ , direct-resolved (resolved-direct) are compatible with direct events in ep, and double-resolved are concentrated at small  $x_\gamma^\pm$  — suggesting a cut at low  $x_\gamma^+$  and  $x_\gamma^-$  to separate double-resolved from single-resolved events.

The SaS 2D distribution gives, with  $Q_{1,2}^2 < 0.8 \text{ GeV}^2$ , a large double-resolved contribution, dominated by the VMD-VMD events. Similarly, direct-VMD events dominate the single-resolved contribution. The effective parameter  $p_{\perp,\text{min}}^{\text{MI}}$  sets the amount of multiple interactions for the VMD component. The results shown in this section are sensitive to the choice of  $p_{\perp,\text{min}}^{\text{MI}}$ , here chosen to  $1.4 \text{ GeV}$ , which is the default in PYTHIA.

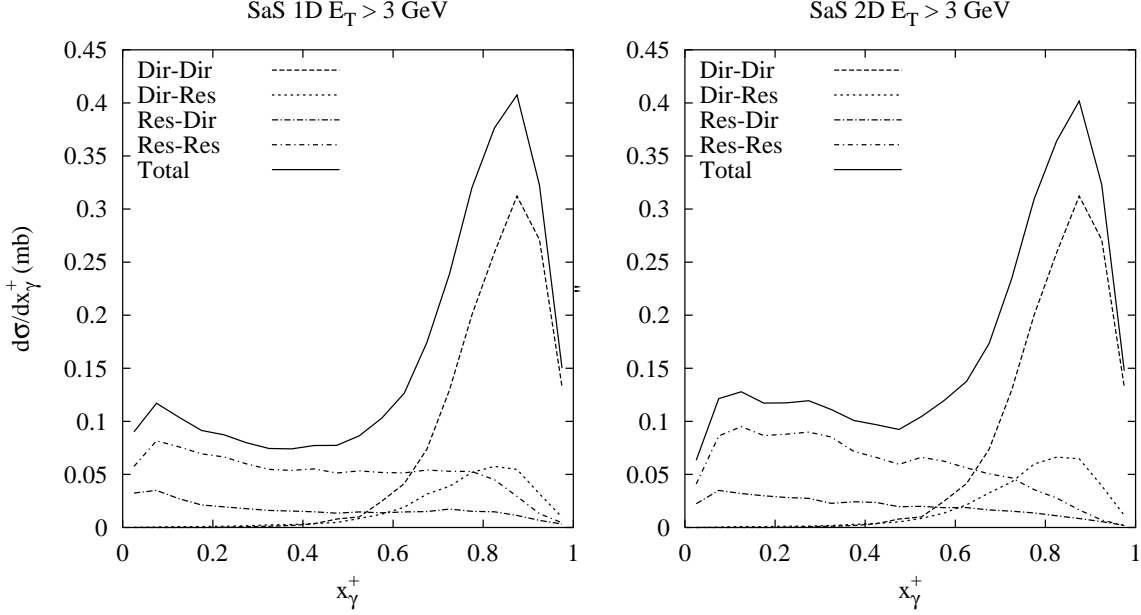


Figure 7: The  $x_\gamma^+$  distribution for the direct and resolved photon components.  $p_\perp^{\text{parton}} = 1.5$  GeV,  $E_\perp^{\text{jet}} > 3$  GeV,  $0.01 < y_{1,2} < 0.99$ ,  $Q_{1,2}^2 < 0.8$  GeV<sup>2</sup> and  $\sqrt{s_{e^+e^-}} = 133$  GeV.

### 3.1.4 Scale Choice in Parton Distributions

To show the dependence on the choice of scale  $\mu^2$  in parton distributions we will study ep events, with direct and resolved events treated separately. Three extreme choices of scales  $\mu_1^2 = p_\perp^2$ ,  $\mu_5^2 = p_\perp^2 + Q^2$  and  $\mu_6^2 \approx 2p_\perp^2$  are compared. For simplicity, we stay with the  $p_\perp$  distribution of the hard scattering  $2 \rightarrow 2$  subprocess, i.e. avoid hadronization, multiple interactions, initial- and final-state bremsstrahlung and jet clustering effects.

In Fig. 8, the  $d\sigma_{\text{ep}}/d\log_{10}(p_\perp/(1\text{GeV}))^2$  distribution for the different scale choices are compared at two different photon virtualities,  $Q^2 \approx 1$  GeV<sup>2</sup> and  $Q^2 \approx 10$  GeV<sup>2</sup>. For the low- $Q^2$  case, their differences are most pronounced for resolved events and the results are in decreasing order in accordance with the scale choice;  $\mu_6$ ,  $\mu_5$  and  $\mu_1$ . Here the anomalous component is the dominant one, explaining the difference between the SaS 1D and the SaS 2D distributions. For direct events, only a rather mild scale-breaking of the proton distributions enters. Since small- $x$  values dominate, where distributions increase with  $\mu^2$ , the  $\mu_6$  scale should give the largest result but the difference from the other two are within errors.

For  $Q^2 \approx 10$  GeV<sup>2</sup>, direct events dominate. The resolved results can be divided into two regions;  $p_\perp^2 < Q^2$  and  $p_\perp^2 > Q^2$ . Remember that the  $\mu_5$  scale imply that the resolved component will not vanish even when  $p_\perp^2 < Q^2$  as can be seen in Fig. 8. With the  $\mu_6$  scale, the evolution range decreases with  $p_\perp^2$  and finally suppresses resolved photons. The  $\mu_1$  scale does not allow resolved photons when  $p_\perp^2 < Q^2$ . (The tiny tail of such events comes from charm production, where actually  $\mu_1^2 = p_\perp^2 + m_c^2$  is used rather than only  $p_\perp^2$ .) The results with the  $\mu_5$  and  $\mu_6$  scales are, of course, in agreement when  $p_\perp^2 \approx Q^2$  and in the tail of the  $p_\perp$  distribution the  $\mu_6$  scale gives the bigger cross section. At large  $Q^2$  values, the difference between the two photon parton distributions are reduced. For direct events the  $\mu_5$  scale is larger than the  $\mu_6$  one at low  $p_\perp^2$  but smaller at high  $p_\perp^2$ ; a

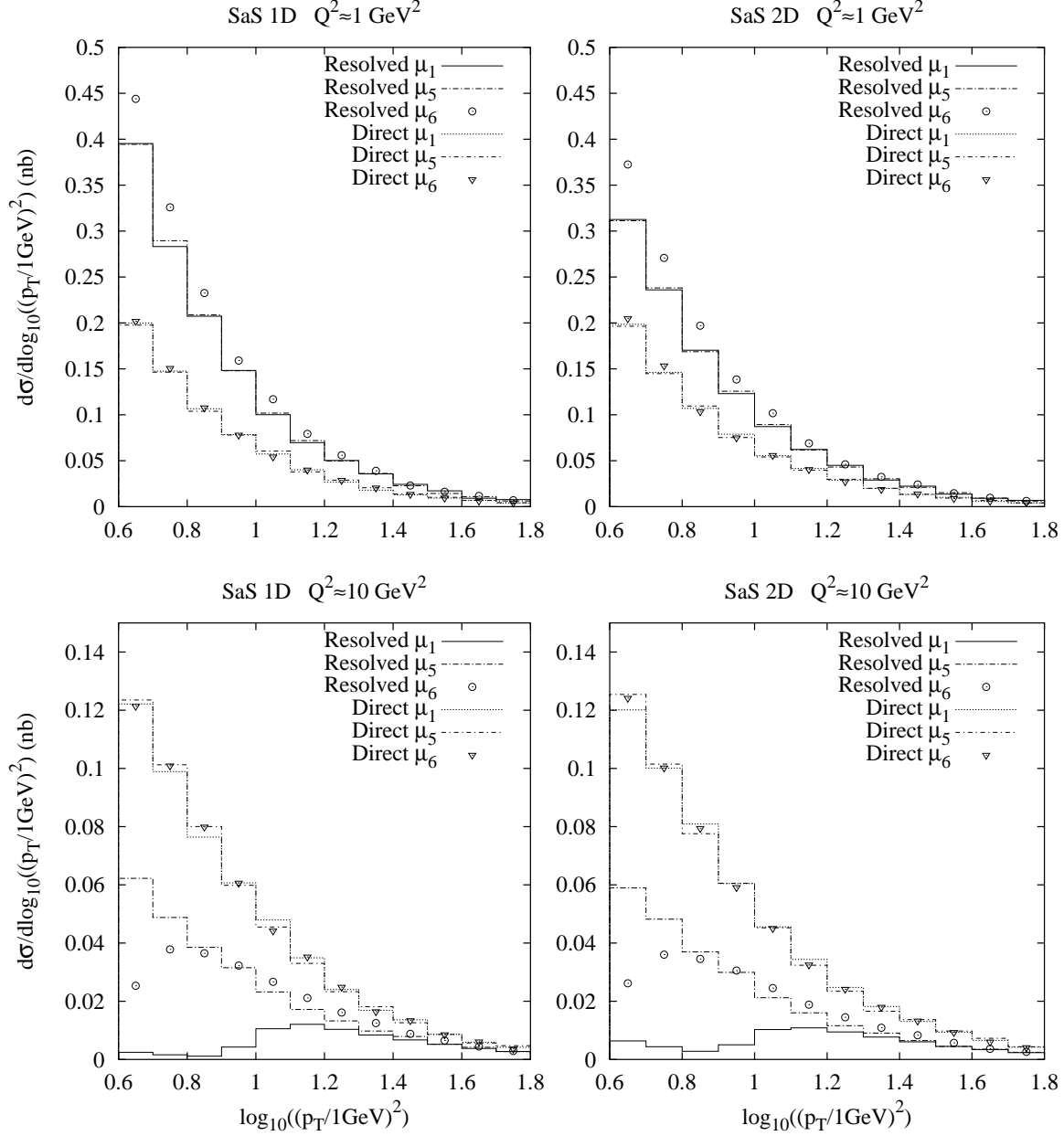


Figure 8: The  $d\sigma_{\text{ep}}/d\log_{10}(p_{\perp}/(1\text{GeV}))^2$  cross section for different  $\mu_i$  scales with  $Q^2 \approx 1 \text{ GeV}^2$  and  $Q^2 \approx 10 \text{ GeV}^2$ ,  $\sqrt{s_{\text{ep}}} \simeq 300 \text{ GeV}$ .

corresponding pattern is expected to be seen in the cross section (again, small- $x$  values dominate). However, differences are small.

### 3.2 Comparisons with Data

In this section the model is compared with data. We will not make a detailed analysis of experimental results but use it to point out model dependences and to constrain some model parameters. Where applicable, the HzTool [32] routines will be used for the comparison with data.

$2 \rightarrow 2$  parton interactions normally give rise to 2-jet events. In leading-order QCD,

the jets are balanced in transverse momenta in the centre of mass frame of the  $\gamma^*p/\gamma^*\gamma^*$  subsystem. Various effects, such as primordial  $k_\perp$ , initial- and final-state bremsstrahlung, etc., tend to spoil this picture. This increases the  $d\sigma/dp_\perp$  spectrum at any fixed  $p_\perp$ , since jets can be boosted up from lower  $p_\perp$ . It is here important to remember that  $d\sigma/dp_\perp$  is dropping steeply with increasing  $p_\perp$ , since the matrix elements described in section 2.2 are divergent for  $p_\perp \rightarrow 0$ . Even a symmetric smearing of jet  $p_\perp$ , i.e. with shifts  $+\delta p_\perp$  and  $-\delta p_\perp$  equally probable, would thus increase  $d\sigma/dp_\perp$ : the jets shifted upwards would migrate into a region less populated than those shifted downwards, and therefore proportionately have a larger impact. Additionally, the smearing is not symmetric, but normally shifts one jet upwards while the other may be shifted in either direction. (This holds for primordial  $k_\perp$  and initial-state radiation, while final-state radiation tends to shift both jets downwards.) In the generation procedure, the divergences are avoided by the introduction of a lower cut,  $p_{\perp,\min}^{\text{parton}}$ , below which parton scatterings are not considered. In order to study jets above some  $p_{\perp,\min}^{\text{jet}}$ , a  $p_{\perp,\min}^{\text{parton}} < p_{\perp,\min}^{\text{jet}}$  is required. Stable results are obtained when a hard scattering with  $p_\perp^{\text{parton}} = p_{\perp,\min}^{\text{parton}}$  for the incoming partons do not produce any jets with  $p_\perp$  above  $p_{\perp,\min}^{\text{jet}}$ . Typically  $p_{\perp,\min}^{\text{parton}} = \frac{1}{2}p_{\perp,\min}^{\text{jet}}$  or less is required.

### 3.2.1 Dijets at HERA

Dijet angular distributions in photoproduction and deep inelastic scattering have been studied at HERA [31]. In the center of mass system of the two highest transverse energy jets (which are restricted to have a transverse energy above a certain value) the angle  $\theta^*$  between the jets and the beam axis is expected to be distributed differently depending on whether or not the photon is resolved. The leading-order direct QCD graphs, boson-gluon fusion and QCD Compton, have spin-1/2 quark propagators leading to an angular dependence proportional to  $1/\hat{t} \propto (1 - |\cos \theta^*|)^{-1}$ . (The jets are generally not distinguishable so the absolute value of  $\cos \theta^*$  cannot be measured.) On the contrary, the resolved processes are dominated by *Rutherford type* scatterings involving a t-channel gluon:  $qq' \rightarrow qq'$ ,  $qg \rightarrow qg$  and  $gg \rightarrow gg$ . These thus give an angular dependence proportional to  $1/\hat{t}^2 \propto (1 - |\cos \theta^*|)^{-2}$  i.e. the dijet angular distribution is expected to rise steeper with  $|\cos \theta^*|$  for resolved processes than for direct ones.

As discussed in the introduction and in section 3.1.3, with a cut in  $x_\gamma^{\text{obs}}$  it is possible to make a separation between events that are likely to be direct from those that are likely to be resolved events. An example of this is shown in Fig. 9 where direct and resolved events generated by PYTHIA is compared with results presented by the ZEUS Collaboration [31], with a good agreement in the shape of the distributions. The plots were produced by using the HzTool package.

In the analysis of the ZEUS Collaboration a cut  $x_\gamma^{\text{obs}} < 0.75$  was used to classify the photon as resolved while for  $x_\gamma^{\text{obs}} > 0.75$  it was classified as a direct photon. Of the events classified as having a direct photon a significant contribution comes from events with an anomalous fluctuation of the photon. This is well understood since, in this component, the quark (antiquark) often carries a large fraction of the original photon momentum. The two jets are then likely to be produced at small scattering angles  $\theta^*$  as described by the matrix elements with gluon exchange. Using the SaS 1D parton distribution, the anomalous component is important for either classification, whereas the VMD part is highly suppressed and negligible by the  $x_\gamma^{\text{obs}} > 0.75$  cut. For SaS 2D, the VMD contribution is small for events classified as direct but of equal importance as the anomalous part for  $x_\gamma^{\text{obs}} < 0.75$ . The choice of scale  $\mu_i$  is not crucial at this low  $Q^2$  values,

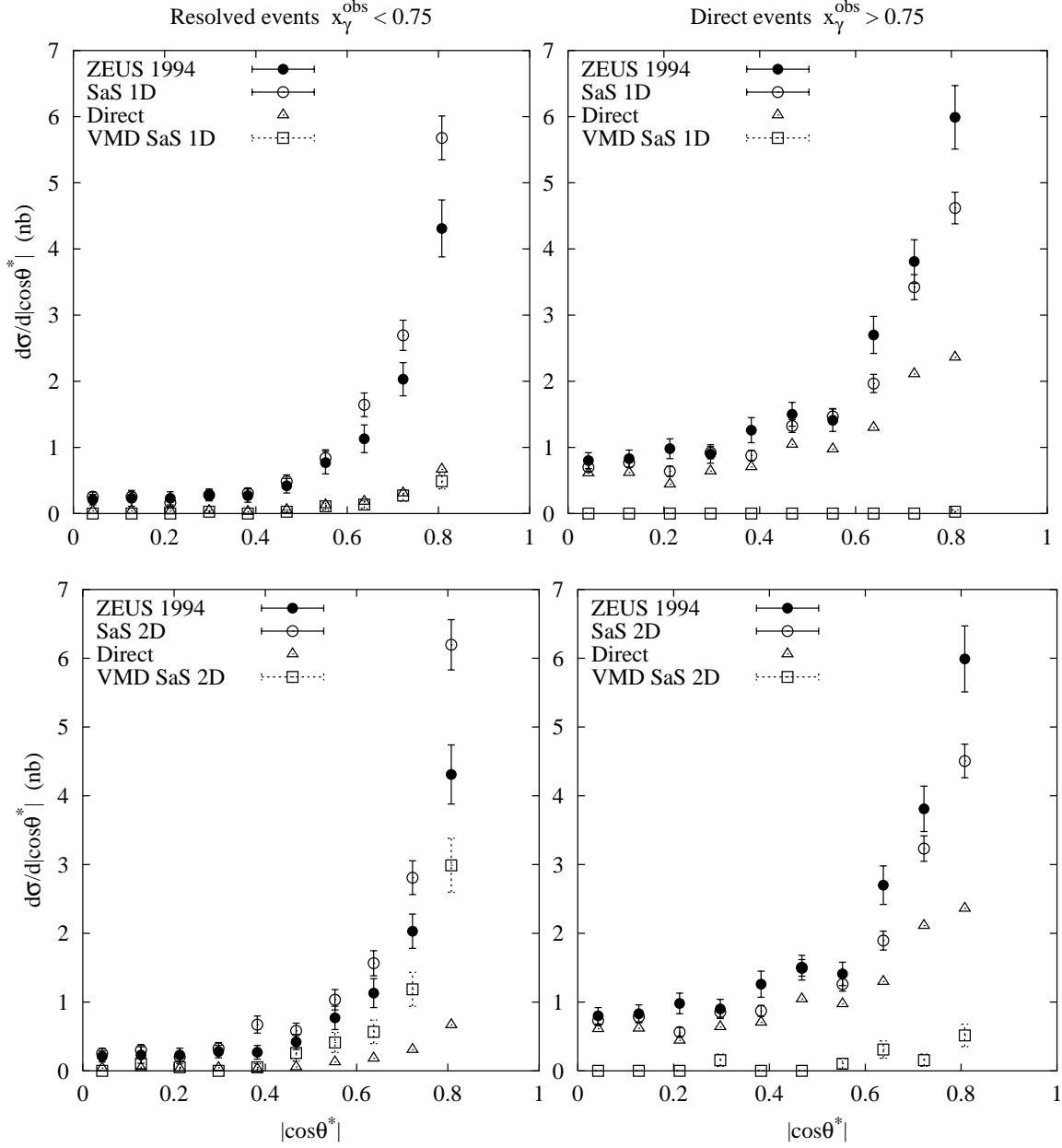


Figure 9: The dijet angular cross section  $d\sigma/d|\cos\theta^*|$  for resolved ( $x_\gamma^{\text{obs}} < 0.75$ ) and direct ( $x_\gamma^{\text{obs}} > 0.75$ ) processes.  $\theta^*$  is the jet scattering angle w.r.t. the beam axis measured in the dijet centre of mass system.  $Q^2 < 4 \text{ GeV}^2$  and  $0.25 < y < 0.8$ . The SaS 1D and SaS 2D curves give the total contribution from the resolved and direct components; the VMD and direct components are also shown separately. The anomalous contribution can be obtained by subtracting the direct and the VMD contribution from the full one.

the  $\mu_3$  scale is used and the results with  $\mu_5$  are within errors.

The possibility for the incoming electron to emit extra photons, that may go undetected, is not taken into account by the model. This effect decreases the lepton energy; hence the photon energy calculated here would be overestimated. A simple estimation of these effects give corrections to the photon energy at the percent level. The consequence

would be that the given  $x_\gamma^{\text{obs}}$  distribution will be shifted towards higher values. An inclusion of such effects would shuffle some of our resolved events into the direct category, thus improving the description of the relative amounts. This could be solved by using lepton-inside-lepton structure functions, though the implementation of it is postponed for the future.

From these observations it is tempting to conclude that a cut in  $x_\gamma^{\text{obs}}$  does not so much separate events with the resolved anomalous component (perturbatively calculable fluctuation) of the photon from the direct component, but rather separates it from the VMD component (non-perturbative fluctuation) of the photon. This statement is true to leading order but the anomalous fluctuation contain pieces that a next-to-leading-order calculation of the direct component would give. Hence, in this sense also anomalous events can be considered as a contribution from the direct component making the  $x_\gamma^{\text{obs}}$  well suited to separate the direct from the resolved component. Nevertheless, the classification of the photon into different components used throughout in this paper is based on the leading order description, viewing the anomalous fluctuation as a resolved photon.

### 3.2.2 Inclusive ep Jet Cross Sections

Inclusive ep jet cross sections have been measured by the H1 collaboration [33] in the kinematical range  $0 < Q^2 < 49 \text{ GeV}^2$  and  $0.3 < y < 0.6$ . The differential jet cross sections  $d\sigma_{\text{ep}}/dE_\perp^*$ ,  $d\sigma_{\text{ep}}/d\eta^*$  and the inclusive  $\gamma^*p$  jet cross section in Fig. 10, 11 and 12 respectively, were produced with the HzTool package. The  $E_\perp^*$  and  $\eta^*$  are calculated in the  $\gamma^*p$  centre of mass frame where the incident proton direction corresponds to positive  $\eta^*$ .

For  $d\sigma_{\text{ep}}/dE_\perp^*$  and  $d\sigma_{\text{ep}}/d\eta^*$  data is available in nine different  $Q^2$  bins, four of them are shown here with similar results for the intermediate bins. The SaS 1D parton distribution together with a few different  $\mu_i$  scales;  $\mu_1$ ,  $\mu_3$ ,  $\mu_5$  and  $\mu_6$ , are used to model the resolved photon component. The other choices of scales,  $\mu_2$  and  $\mu_4$ , interpolates between these results.

In the highest  $Q^2$  bin the direct component is the dominant contribution; the virtuality of the photon is for most events of the order of or larger than the transverse momenta squared,  $Q^2 \gtrsim p_\perp^2$ . However, the resolved component is not negligible and all the scales  $\mu_i$ , except  $\mu_1$ , depend on the photon virtuality. This gives a larger resolved component in this region as compared to the conventional choice,  $\mu_1 = p_\perp$ . In the low- $Q^2$  bin the  $\mu_i$  scales do not differ much from  $p_\perp$ , i.e. the results are not sensitive to the scale choice  $\mu_i$ . The exception is  $\mu_6$ , which there overshoots the data. The  $\mu_4^2 = p_\perp^2 + Q^2/2$  scale (not shown) gives nice agreement with data for all different  $Q^2$  bins.

Since the VMD part dies out quickly with increasing photon virtuality, multiple interactions will only be visible at low  $Q^2$  (multiple interactions for the anomalous component is not in the model so far). The anomalous component dominates over the VMD component already at  $1 \text{ GeV}^2$ . Therefore, multiple interactions for the VMD component can safely be neglected for the distributions shown in this section.

Changing the photon parton distribution from SaS 1D to SaS 2D will give a slightly lower result for the low- $Q^2$  bins, Fig. 13. The GRS LO [22] parton distribution gives a similar result as the other two. It has a restricted regime of validity,  $Q^2 \ll \mu^2$  (implemented as  $5Q^2 < \mu^2$ ) and  $Q^2 < 10 \text{ GeV}^2$ . Therefore, it is absent in the high- $Q^2$  bin, and some regions of phase space are cut out in the low- $E_\perp^*$  bins and in the  $\eta^*$  distributions ( $5Q^2 \gtrsim (E_\perp^*)^2$ ). One could imagine larger differences for virtual-photon parton distribu-

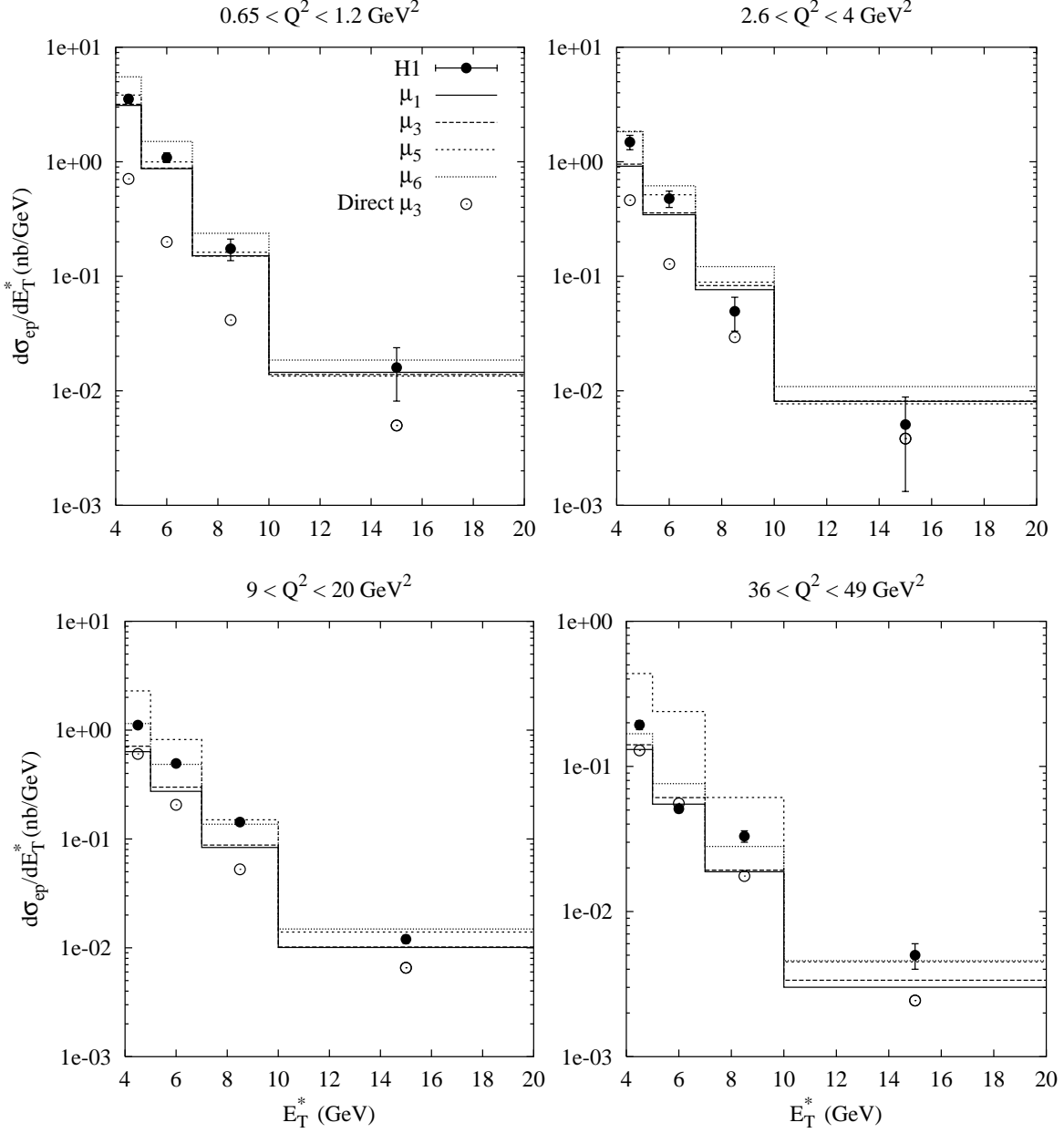


Figure 10: The differential jet cross section  $d\sigma_{\text{ep}}/dE_{\perp}^*$  for jets with  $-2.5 < \eta^* < -0.5$  and  $0.3 < y < 0.6$ .

tions that from the onset are more different, so the good SaS/GRS agreement is somewhat fortuitous. Using a parton distribution for a real photon cannot describe the  $Q^2$  dampening in the distributions shown in this section. As an example of this the GRV LO [34] distribution has been used; the change here is solely from the photon flux.

Using CTEQ 3L instead of GRV 94 LO as the proton parton distribution reduces the result in some  $E_{\perp}^*$  and  $\eta^*$  bins by half, Fig. 14. The GRV 94 HO parton distribution give a slightly lower result (as compared to GRV 94 LO). The differences mainly come from the gluon distributions, that are not yet so well constrained from data. In the modeling of the parton distributions, it is a deceptive accident that the more well-known proton parton distribution gives a larger uncertainty than the photon one. It offers a simple

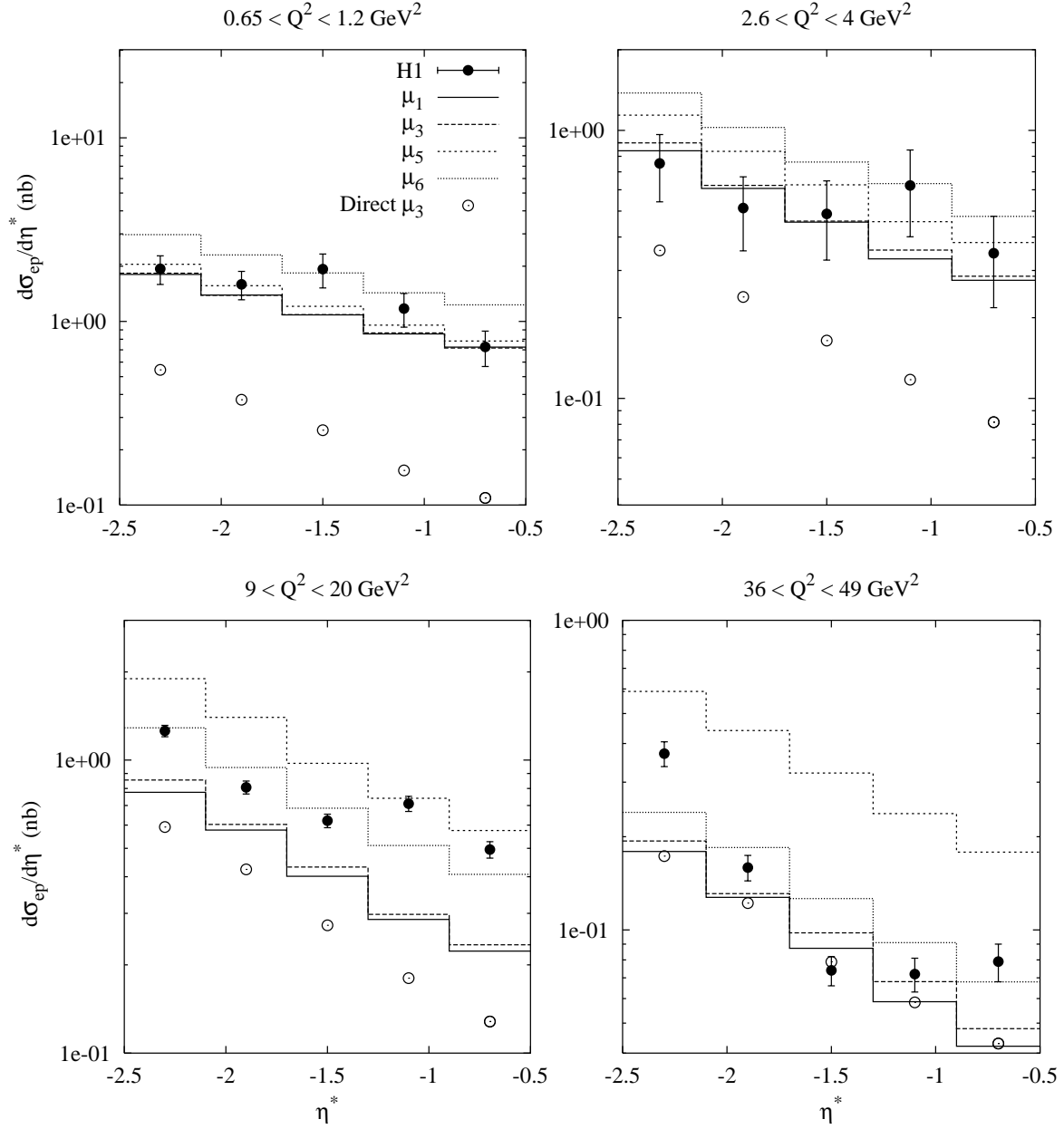


Figure 11: The differential jet cross section  $d\sigma_{\text{ep}}/d\eta^*$  for jets with  $E_{\perp}^* > 5$  GeV and  $0.3 < y < 0.6$ .

example that also phenomenology of other areas may directly influence the interpretation of photon data.

### 3.2.3 Inclusive $\gamma^*\gamma^*$ Jet Cross Sections

The OPAL collaboration has measured inclusive one-jet and two-jet cross sections in the range  $|\eta^{\text{jet}}| < 1$  and requiring  $E_{\perp}^{\text{jet}}$  to be larger than 3 GeV [35]. The centre of mass energies were 130 and 136 GeV. In the analysis, a cone jet algorithm was used with a cone radius  $R = 1$  and  $E_{\perp, \text{min}}^{\text{jet}} = 2$  GeV; differences in the application of this algorithm may affect the results (we used the PXCONe algorithm from HzTool). The two-jet cross sections were obtained by measuring events with at least two jets, and then using only



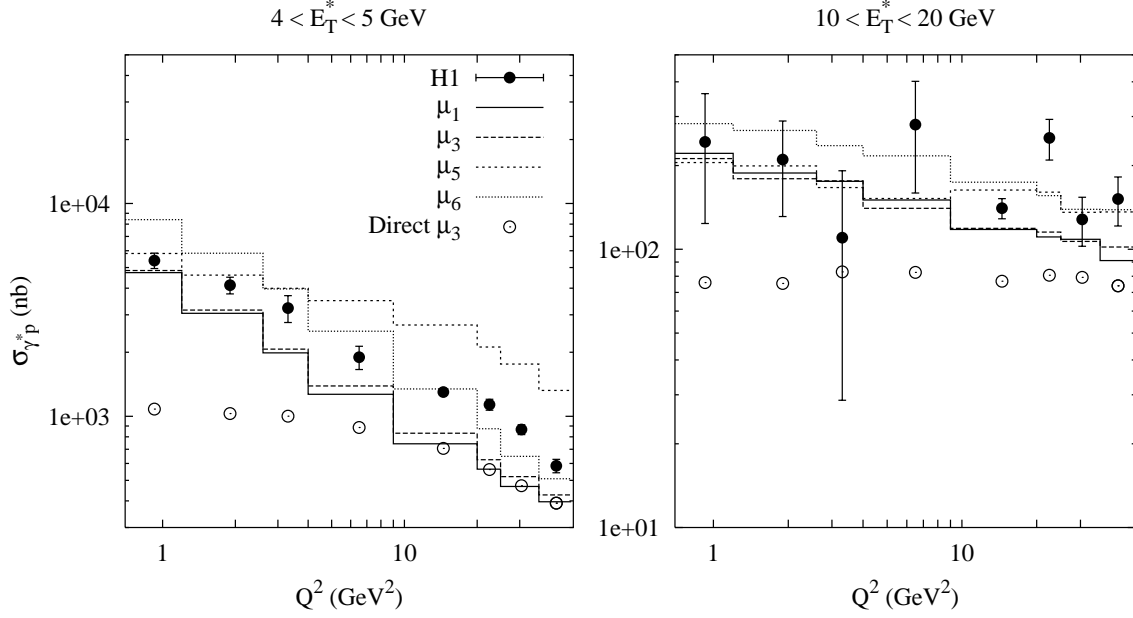


Figure 12: The inclusive  $\gamma^*p$  jet cross section  $\sigma_{\gamma^*p}$  for jets with  $-2.5 < \eta^* < -0.5$  and  $0.3 < y < 0.6$ .

the two hardest jets. In Figs. 15–18, the inclusive jet cross sections as a function of  $E_{\perp}^{\text{jet}}$  or  $\eta^{\text{jet}}$  are shown, with events generated at  $\sqrt{s_{\text{ee}}} = 133$  GeV. The anti-tagging conditions at this energy corresponds to a  $Q_{\text{max}}^2 = 0.8$  GeV<sup>2</sup>. Due to migration effects  $p_{\perp,\text{min}}^{\text{parton}}$  was chosen to 1.5 GeV, and  $p_{\perp,\text{min}}^{\text{MI}} = 1.4$  GeV. The symmetric cuts used gives no difference between the two single-resolved contributions, instead the direct-VMD (VMD-direct) and direct-anomalous (anomalous-direct) contributions is shown together with the direct and double-resolved ones.

At low  $E_{\perp}^{\text{jet}}$  the double-resolved events are dominating and at larger  $E_{\perp}^{\text{jet}}$  it is the direct processes since more energy goes into the hard scattering in the latter case. For single-resolved events, the SaS 1D VMD component dies out much quicker with increasing  $E_{\perp}^{\text{jet}}$  than the SaS 2D one which is comparable with the direct-anomalous events at high  $E_{\perp}^{\text{jet}}$ . For both cases, at high  $E_{\perp}^{\text{jet}}$ , the direct-anomalous components give the same order of magnitude contribution to the cross section as the double-resolved events. The biggest difference between the two parton distributions can be seen at low  $E_{\perp}^{\text{jet}}$  and for the  $|\eta^{\text{jet}}|$  distributions, where the double-resolved events dominates; it is a reflection of the difference in normalization among the contributions. For the SaS 2D case, this kinematical region makes the VMD component more important than the anomalous one; as a consequence multiple interactions play an important role. The double-resolved contribution for SaS 2D without multiple interaction is half of the one shown here. Clearly, for the SaS 1D case the opposite is true: the importance of the components are reversed. In the region of high  $E_{\perp}^{\text{jet}}$ , where the direct events dominate, the model is undershooting data. On the other hand, there is nice agreement with data for the  $|\eta^{\text{jet}}|$  distribution when using SaS 2D.

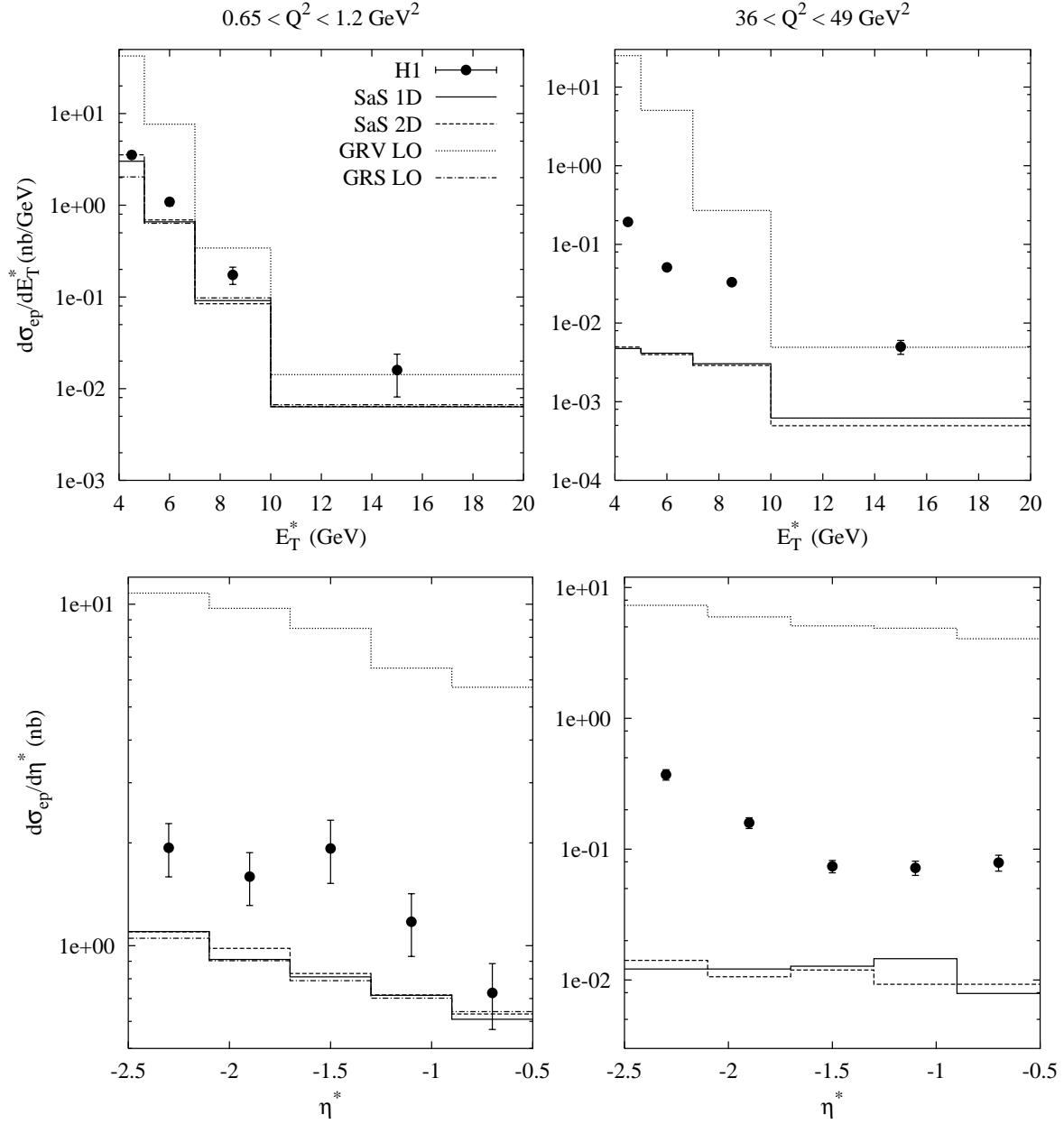


Figure 13: The differential jet cross sections  $d\sigma_{ep}/dE_\perp^*$  and  $d\sigma_{ep}/d\eta^*$  for jets with  $-2.5 < \eta^* < -0.5$  and  $0.3 < y < 0.6$ . Only resolved events are used to show the sensitivity to the photon parton distribution.

### 3.2.4 Forward Jets in ep

Jet cross sections as a function of Bjorken- $x$ ,  $x_{Bj}$ , for forward jet production (in the proton direction) have been measured at HERA [36]. The objective is to probe the dynamics of the QCD cascade at small  $x_{Bj}$ . The forward jet is restricted in polar angle w.r.t. the proton and the transverse momenta  $p_\perp^{\text{jet}}$  should be of the same order as the virtuality of the photon, suppressing an evolution in transverse momenta. If the jet has a large energy fraction of the proton, there will be a big difference in  $x$  between the jet and the photon vertex,  $x_{Bj} \ll x_{\text{jet}}$ , allowing an evolution in  $x$ . The above restrictions will not eliminate the possibility of having a resolved photon, although the large  $Q^2$  values are not in favour

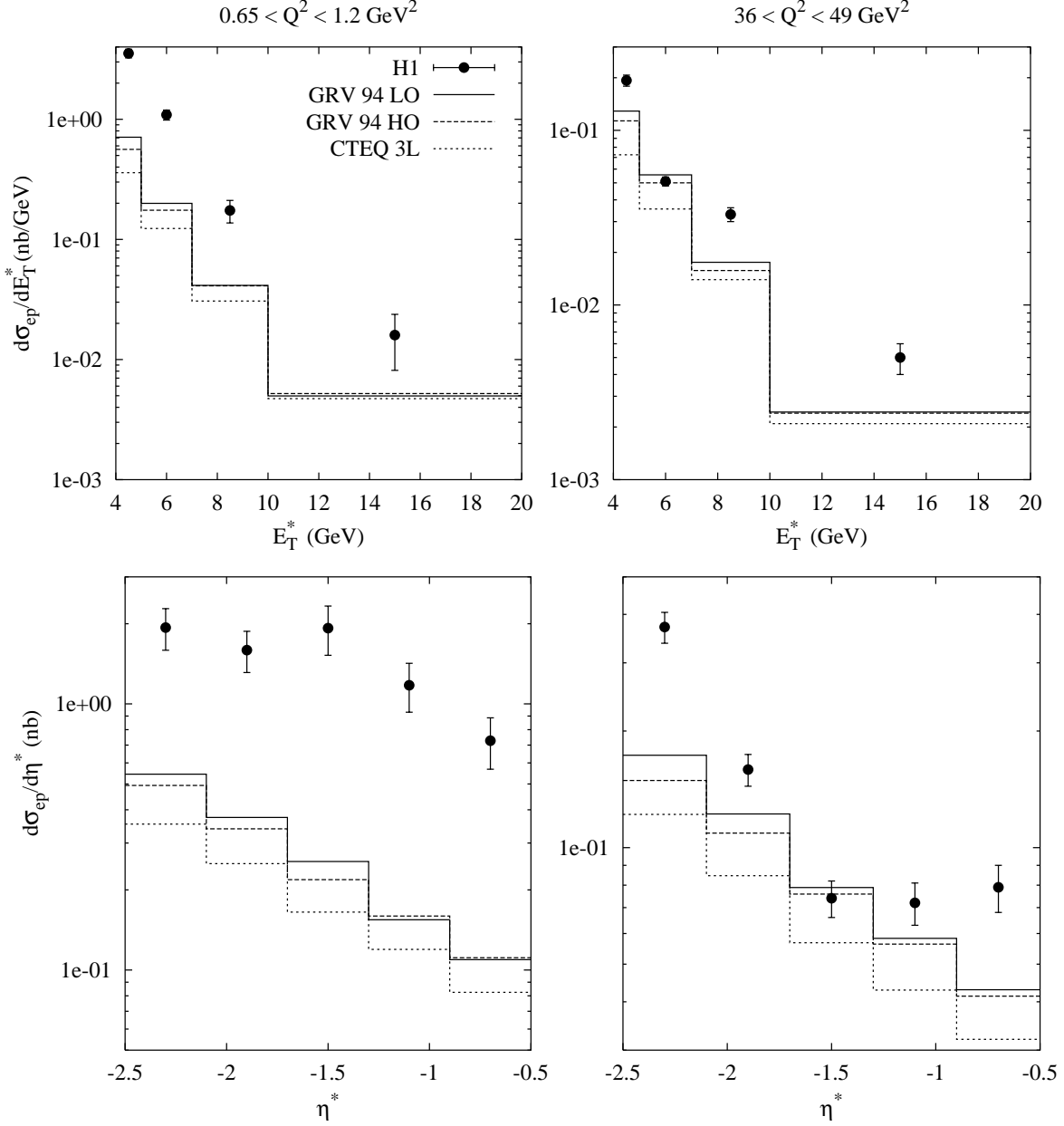


Figure 14: The differential jet cross sections  $d\sigma_{\text{ep}}/dE_{\perp}^*$  and  $d\sigma_{\text{ep}}/d\eta^*$  for jets with  $-2.5 < \eta^* < -0.5$  and  $0.3 < y < 0.6$ . Only direct events are used to show the sensitivity to the proton parton distribution.

of it.

The HzTool routines were used to obtain the results in Fig. 19. Five different scales  $\mu_i$  are shown. A larger forward jet cross section is obtained with a stronger  $Q^2$  dependence, with the scale  $\mu_5^2 = p_{\perp}^2 + Q^2$  in best agreement with data, in general agreement with the conclusions in [24]<sup>3</sup>. The constraint  $(p_{\perp}^{\text{jet}})^2 \simeq Q^2$  gives a large enhancement for the  $\mu_4$  and  $\mu_5$  scales, which are combinations of  $(p_{\perp}^{\text{parton}})^2$  and  $Q^2$ , whereas  $\mu_2$  and  $\mu_3$  have a  $Q^2$

<sup>3</sup>However, we note a not complete agreement in the description of the inclusive jet cross sections. In [24] a different option of the SaS extension to virtual photons was used than here, but we have checked that this cannot be the main reason for the discrepancy.

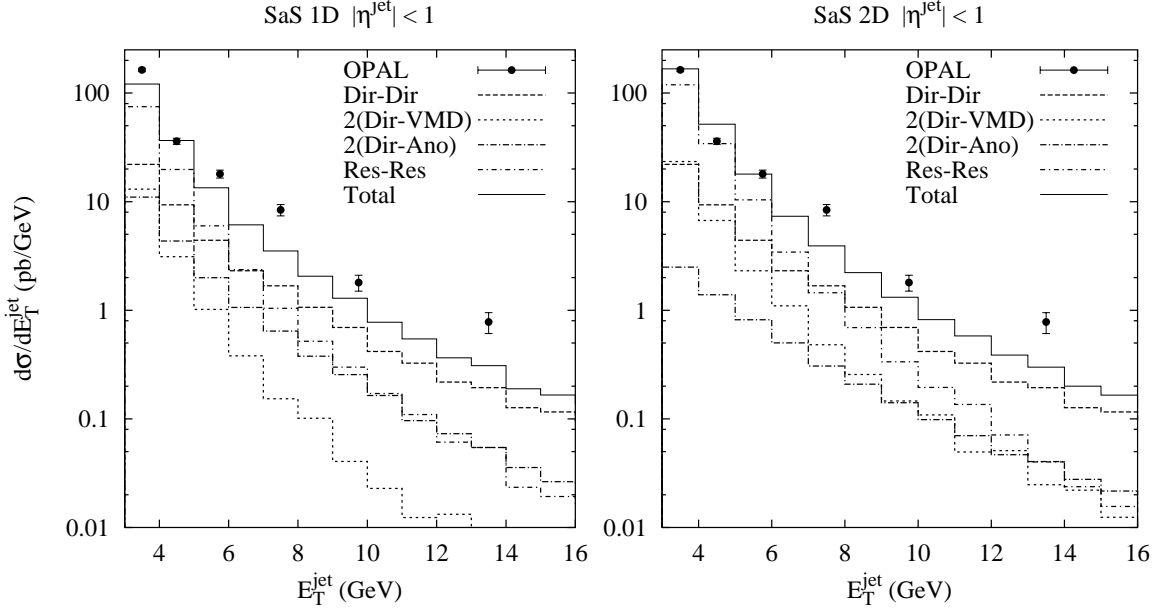


Figure 15: The inclusive one-jet cross section as a function of  $E_{\perp}^{\text{jet}}$  at the centre of mass energies  $\sqrt{s_{e^+e^-}} = 130$  and  $136$  GeV,  $|\eta^{\text{jet}}| < 1$ . The events were generated at a fixed energy of  $\sqrt{s_{e^+e^-}} = 133$  GeV,  $Q_{\text{max}}^2 = 0.8$  GeV<sup>2</sup>,  $p_{\perp,\text{min}}^{\text{parton}} = 1.5$  GeV and  $p_{\perp,\text{min}}^{\text{MI}} = 1.4$  GeV.

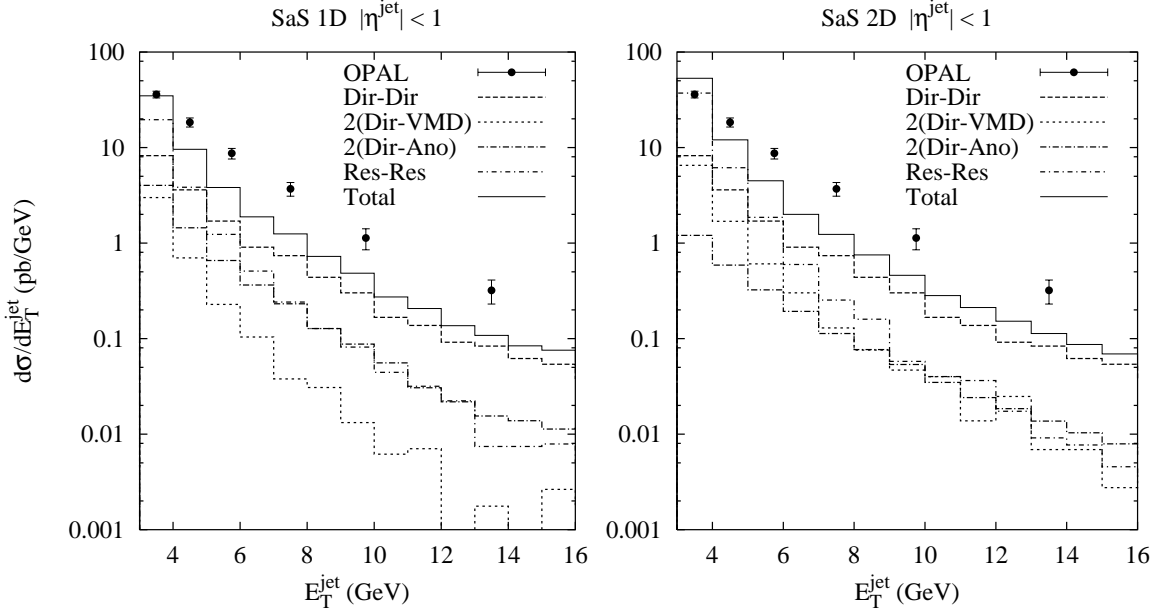


Figure 16: The inclusive two-jet cross section as a function of  $E_{\perp}^{\text{jet}}$ ; for more information see Fig. 15.

dependence that are scaled down by  $\hat{s}$ . The choice of scale does not only affect the resolved photon contribution but also the direct photon, arising from the scale dependence in the proton parton distribution, as seen in Fig. 20. As a check for the direct component, a simple comparison was made between PYTHIA, using the  $\mu_1 = p_{\perp}$  scale and the direct

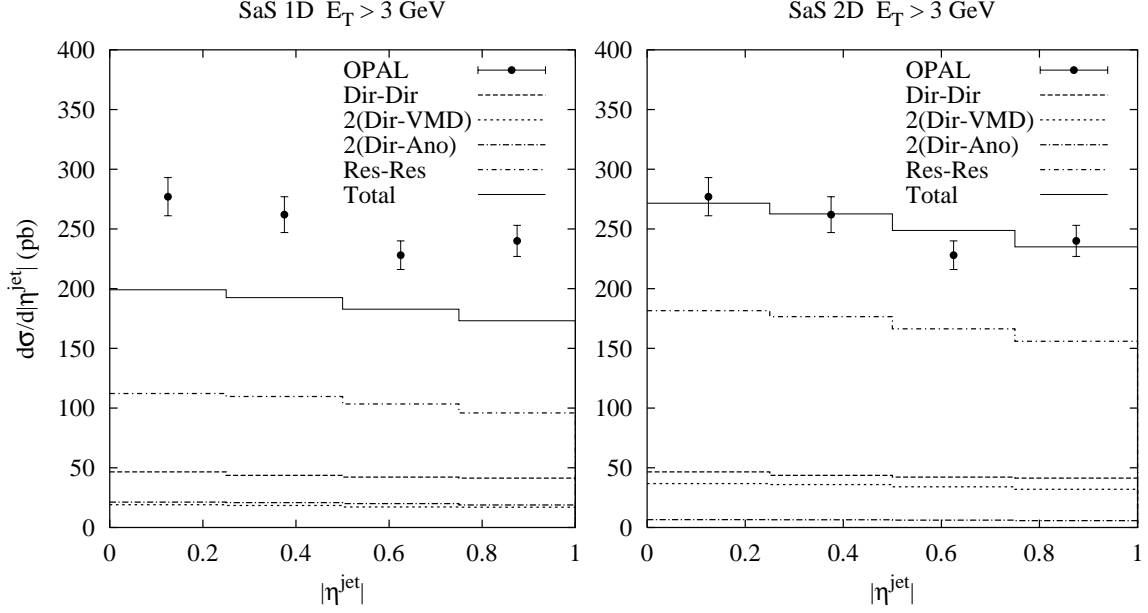


Figure 17: The inclusive one-jet cross section as a function of  $\eta^{\text{jet}}$  at the centre of mass energies  $\sqrt{s_{e^+e^-}} = 130$  and  $136$  GeV,  $E_{\perp}^{\text{jet}} > 3$  GeV. The events were generated at a fixed energy of  $\sqrt{s_{e^+e^-}} = 133$  GeV,  $Q_{\text{max}}^2 = 0.8$  GeV<sup>2</sup>,  $p_{\perp,\text{min}}^{\text{parton}} = 1.5$  GeV and  $p_{\perp,\text{min}}^{\text{MI}} = 1.4$  GeV.

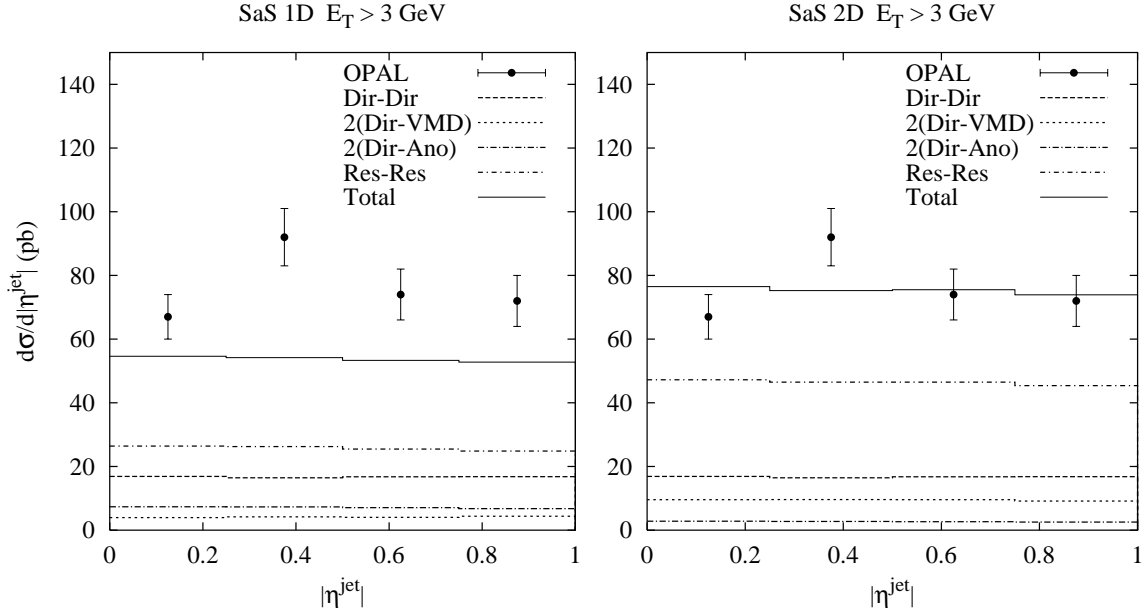


Figure 18: The inclusive two-jet cross section as a function of  $\eta^{\text{jet}}$ ; for more information see Fig. 17.

processes, and LEPTO [7], without soft colour interactions, giving similar results. The rather large  $Q^2$  values,  $Q^2 \simeq (p_{\perp}^{\text{jet}})^2$ , suppresses VMD photons and favours the SaS 1D distribution which is the one used here, though the difference is small.

Note that the  $\mu_6$  scale undershoots the forward jet cross section data and overshoots

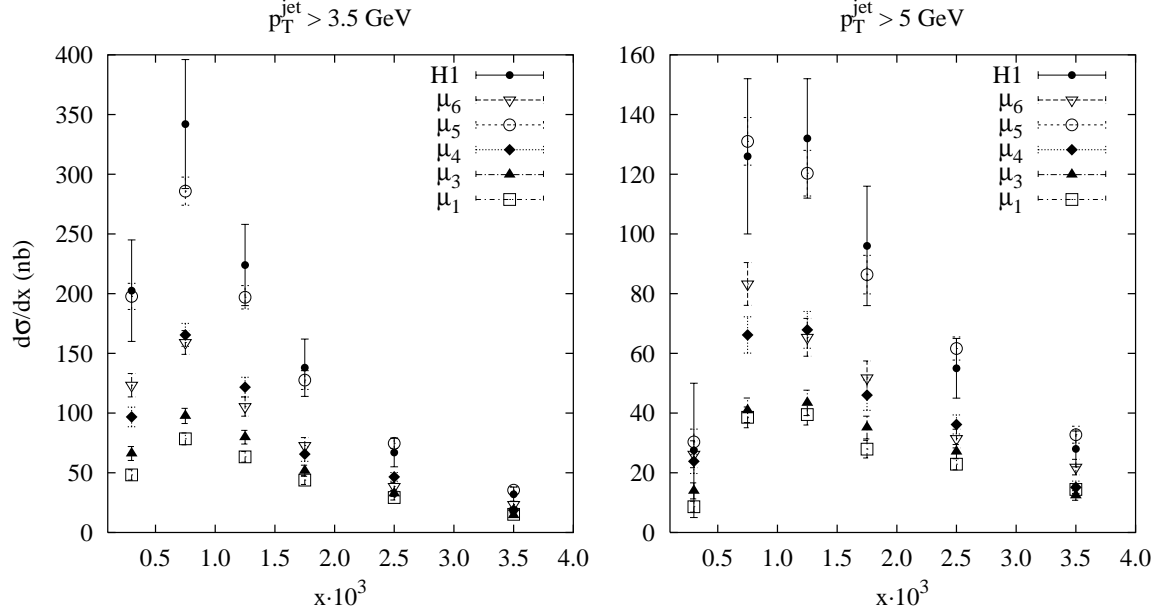


Figure 19: Forward jet cross section as a function of  $x$  compared with H1 data (with statistical and systematic uncertainties added in quadrature). Five different scales are shown at two different  $p_{\perp}^{\text{jet}}$  cuts, 3.5 and 5 GeV.  $x_{\text{jet}} > 0.035$ ,  $0.5 < (p_{\perp}^{\text{jet}})^2/Q^2 < 2$  and  $7^\circ < \theta_{\text{jet}} < 20^\circ$ .

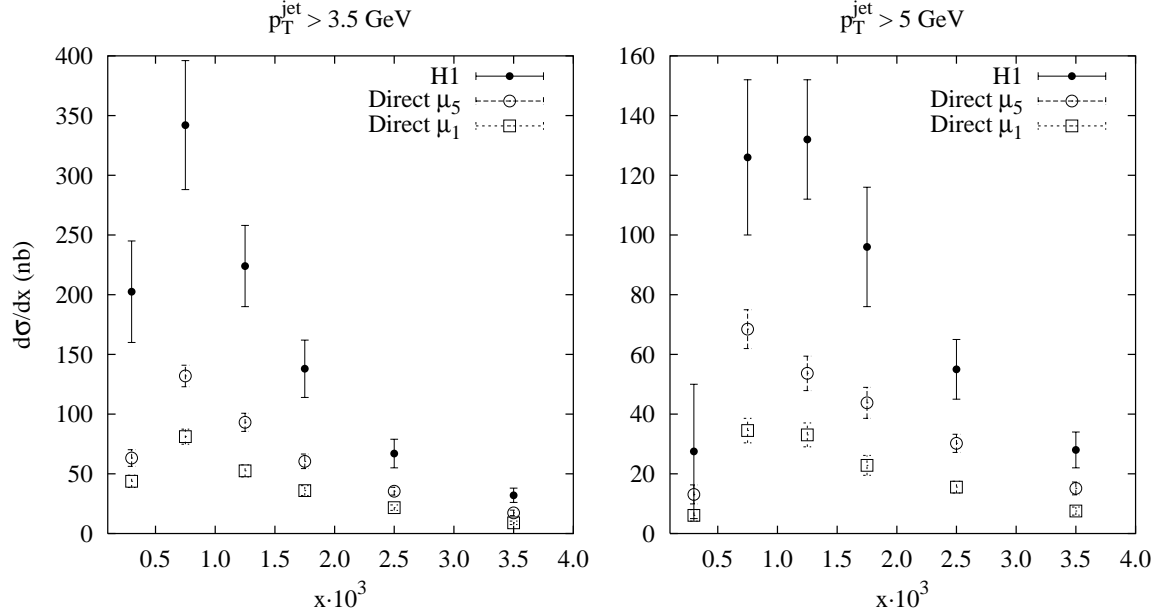


Figure 20: Same as in Fig. 19 but only the direct component is compared with data for two different scale choices.

the inclusive jet distributions at low  $Q^2$ , so it is not a real alternative. As a further check, with more data accumulated and analyzed, the  $(p_{\perp}^{\text{jet}})^2/Q^2$  interval could be split into several subranges which hopefully would help to discriminate between scale choices.

### 3.2.5 Importance of Longitudinal Resolved Photons

In this section we will study the importance of longitudinal resolved photons. The different  $R$ -factors described in section 2.3 will be used to provide some estimates. Of those distributions studied so far, we will concentrate on the  $d\sigma_{\text{ep}}/dE_{\perp}^*$  distributions for inclusive jets and the  $d\sigma_{\text{ep}}/dx$  for forward jet cross sections. A sensible  $Q^2$ -dependent scale choice,  $\mu_3$ , together with the SaS 1D distribution will be used throughout.

With  $a = 1$  the different alternatives are shown in Fig. 21 for the  $d\sigma_{\text{ep}}/dE_{\perp}^*$  distributions together with the result from pure transverse photons, i.e.  $a = 0$ . The importance of the resolved contributions decreases with increasing  $Q^2$ , see Fig. 10, which makes the asymptotic behaviour less crucial. The onset of longitudinal photons governed by the  $R_1$  and  $R_2$  alternatives are favoured whereas the  $R_3$  one overshoots data in the context of the other model choices made here.

In Fig. 22 the same alternatives are shown for the forward jet cross sections. With this scale choice,  $\mu_3$ , none of the longitudinal resolved components (together with the direct contribution) are sufficient to describe the forward jet cross section. The resolved contribution with  $R_3$  is about the same as the one obtained with the scale  $\mu_5^2 = p_{\perp}^2 + Q^2$  (without longitudinal contribution); the difference in the total results originates from the difference in the direct contributions, see Fig. 20. With  $R_1$  and  $a = 1$ , the  $\mu_5$  scale (not shown) overshoots the data, but undershoots in combination with  $\mu_4$ . The  $\mu_4$  scale in combination with  $R_3$  and  $a = 1$  is in nice agreement with data.

The above study indicates, as expected, that longitudinal resolved photons are important for detailed descriptions of various distributions. It cannot by itself explain the forward jet cross section, but may give a significant contribution. Combined with other effects, for example, different scale choices, parton distributions, underlying events, etc. it could give a reasonable description. The model(s) so far does not take into account the difference in  $x$  distribution or the  $k^2$  scale (of the  $\gamma^* \rightarrow q\bar{q}$  fluctuations) between transverse and longitudinal photons. As long as the distributions under study allow a large interval in  $x$  the average description may be reasonable. In a more sophisticated treatment these aspects have to be considered in more detail.

### 3.3 Example of Further Tests: Forward Jets in $e^+e^-$

With the experience of forward jets at HERA, we suggest a similar study at LEP. The optimal kinematical and forward jet constraints have to be set by each collaboration itself; the study here will give the order of magnitude for the cross section and point out uncertainties in the model.

Comparing with forward jets at HERA, one of the leptons will play the role of the proton. Some of the constraints will be taken over directly, kinematic cuts:

$$y > 0.1, \quad E'_e > 11 \text{ GeV}, \quad (46)$$

and jet selection:

$$p_{\perp}^{\text{jet}} > 3.5 \text{ GeV} \quad (47)$$

$$x_{\text{jet}} = \frac{E_{\text{jet}}}{E_e} > 0.035 \quad (48)$$

$$0.5 < \frac{(p_{\perp}^{\text{jet}})^2}{Q^2} < 2 \quad (49)$$

$$3^\circ < \theta_{\text{jet}} < 20^\circ \quad (50)$$

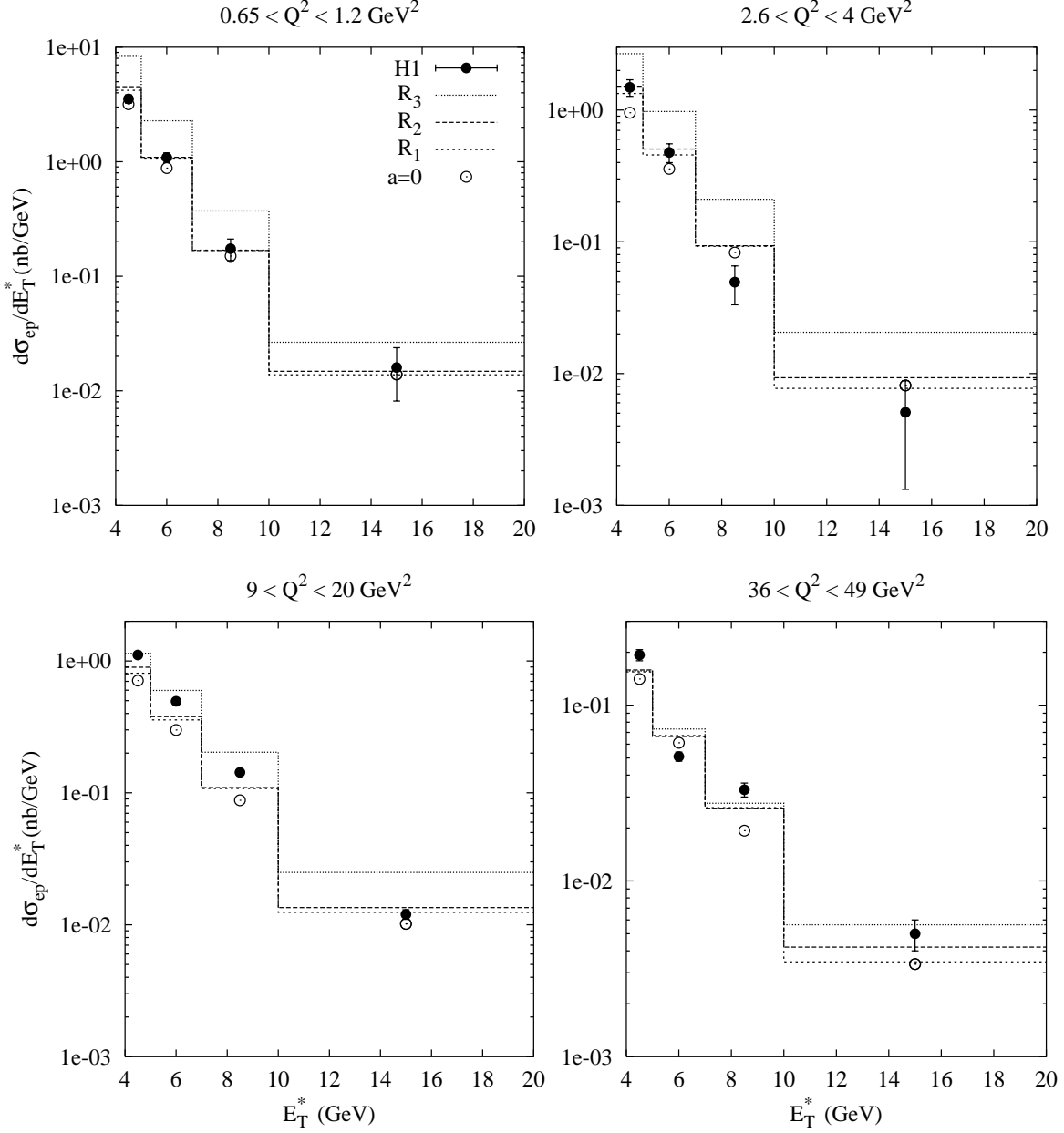


Figure 21: The differential jet cross section  $d\sigma_{\text{ep}}/dE_{\perp}^*$  for jets with  $-2.5 < \eta^* < -0.5$  and  $0.3 < y < 0.6$ .

To fulfill the jet selection one of the leptons has to be tagged in order to know the virtuality of the photon. To obtain a reasonable number of events the other lepton is not tagged, imposing a  $Q_{\text{max}}^2$ , here chosen to  $1.5 \text{ GeV}^2$ . With a centre of mass energy of  $200 \text{ GeV}$ , the smallest accessible  $x_{\text{Bj}} = \frac{Q^2}{ys}$  is around  $10^{-4}$ , where  $Q^2$  and  $y$  is calculated from the tagged electron, omitting the virtuality of the other photon. In a more sophisticated treatment also double-tagged events are analyzed; then one of the photons plays the role of a proton and the forward jet should be defined with respect to one of the photons.

A cone jet algorithm with cone radius  $R = 1$  and  $E_{\perp, \text{min}}^{\text{jet}} = 2 \text{ GeV}$  is used for jet finding. As for the case at HERA, the  $\mu_5$  scale gives the largest forward jet cross section, about twice as large as with the  $\mu_2$  scale, Fig. 23. Most of the differences arise from the double-



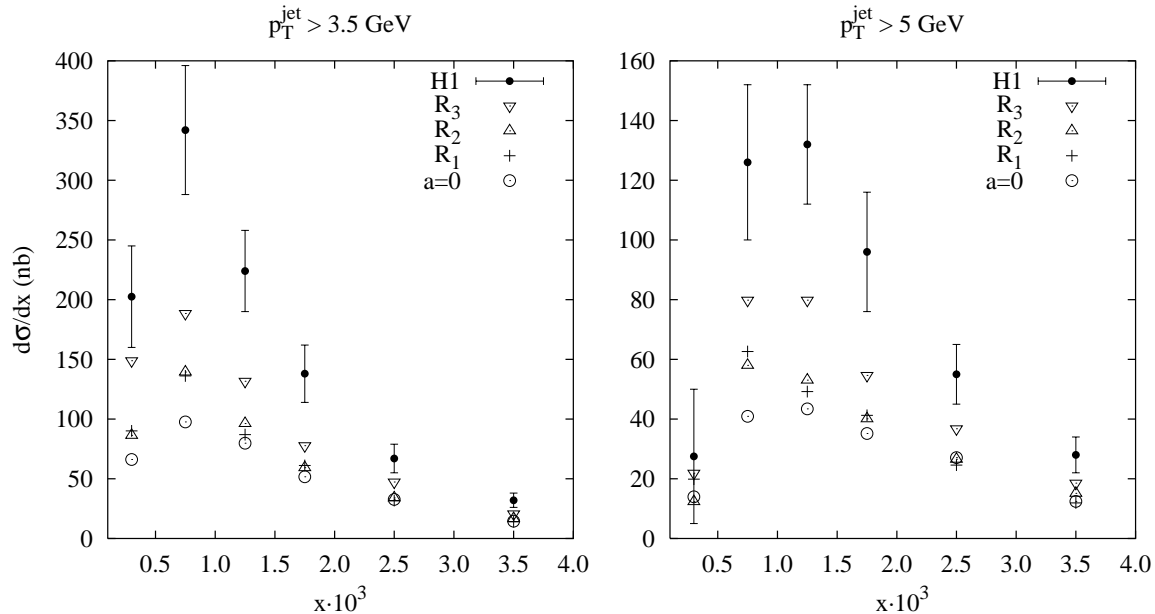


Figure 22: Forward jet cross section as a function of  $x$ .

resolved events. Double-resolved and single-resolved events, where the resolved photon give rise to the forward jet, dominate the forward jet cross section, Fig. 23 and 24. At low  $x$ , for the  $\mu_5$  scale, the double-resolved contribution is close to an order of magnitude larger than the direct one. For the  $\mu_2$  scale it is about a factor of four. As for the case at HERA, the rise of the forward jet cross section at small  $x$  is dominated by resolved photons. A study like this at LEP could be an important cross check for the understanding of resolved photons and that of small- $x$  dynamics.

## 4 Summary and Outlook

The field of photon physics is rapidly expanding, not least by the impact of new data from HERA and LEP. The prospects of building a Linear Collider, with its objective of high-precision measurements and to search for possible new physics, requires an accurate description of photon processes. The plan here is to have a complete description of the main physics aspects in  $\gamma p$  and  $\gamma\gamma$  collisions, which will allow important cross checks to test universality of certain model assumptions. As a step forward, we have in this article concentrated on those that are of importance for the production of jets by virtual photons, and are absent in the real-photon case. While we believe in the basic machinery developed and presented here, we have to acknowledge the many unknowns — scale choices, parton distribution sets (also those of the proton), longitudinal contributions, underlying events, etc. — that all give non-negligible effects. To make a simultaneous detailed tuning of all these aspects was not the aim here, but rather to point out model dependences that arise from a virtual photon.

When  $Q^2$  is not small, naively only the direct component needs to be treated, but in practice a rather large contribution arises from resolved photons. For example, for high- $Q^2$  studies like forward jet cross sections, Fig. 19–20, or inclusive differential jet cross sections, Fig. 10–12. Resolved longitudinal photons are poorly understood and the model presented

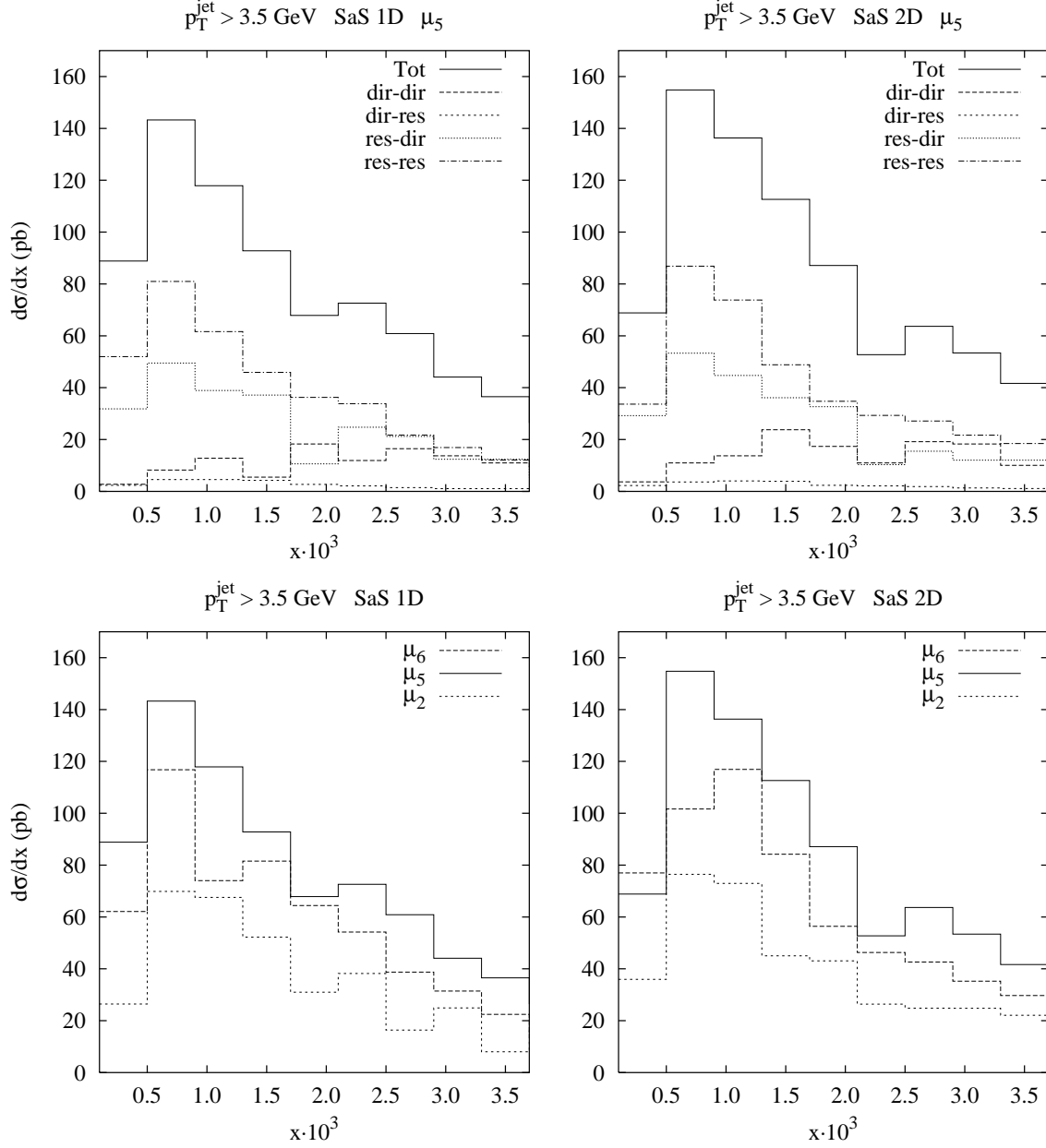


Figure 23: Forward jet cross section as a function of  $x$ .  $p_{\perp}^{\text{jet}} > 3.5$  GeV,  $x_{\text{jet}} > 0.035$ ,  $0.5 < (p_{\perp}^{\text{jet}})^2/Q^2 < 2$  and  $3^\circ < \theta_{\text{jet}} < 20^\circ$ .

here can be used to estimate their importance and get a reasonable global description. Longitudinal effects are in most cases small but of importance for fine-tuning.

In the study of the dijet angular distributions in photoproduction the relative amount of direct and resolved events is not so well described by the model. In the future, this could be improved by using lepton-inside-lepton structure functions.

The inclusive  $\gamma^*\gamma^*$  one-jet and two-jet cross sections are well described except for the high  $E_{\perp}^{\text{jet}}$  region of the  $E_{\perp}^{\text{jet}}$  distribution. In this region, the direct events are dominating. Currently, owing to the lesser flexibility in the modeling of the direct component, we do not see any simple way to improve the model. The factorized ansatz made for the photon flux is expected to be valid in this kinematical range; interference terms are suppressed

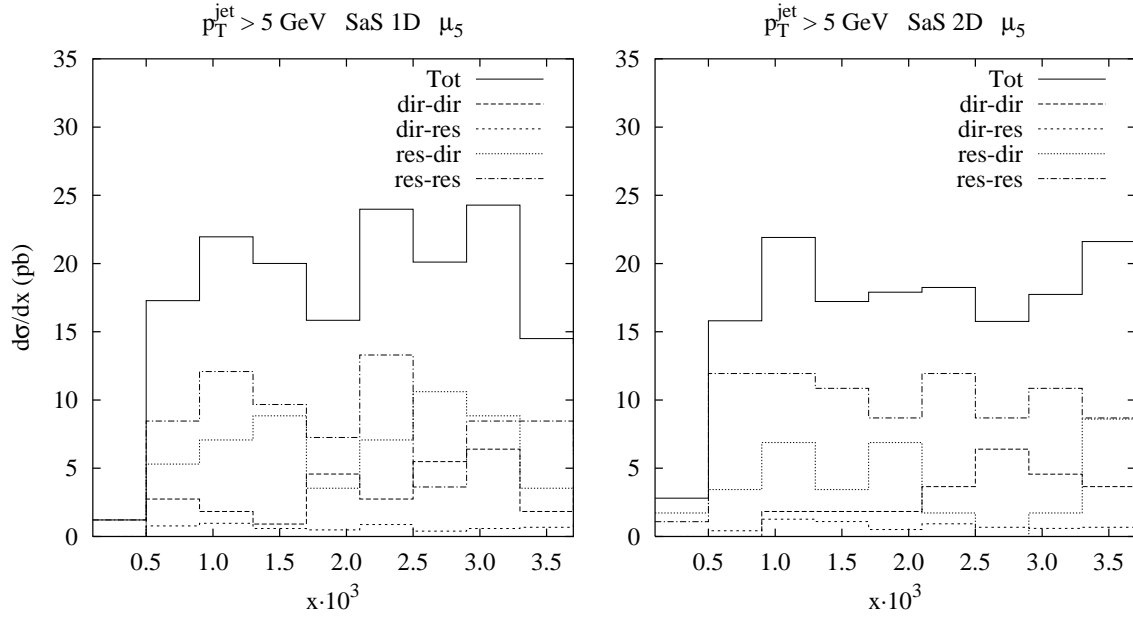


Figure 24: Forward jet cross section as a function of  $x$ .  $p_{\perp}^{\text{jet}} > 5$  GeV,  $x_{\text{jet}} > 0.035$ ,  $0.5 < (p_{\perp}^{\text{jet}})^2/Q^2 < 2$  and  $3^\circ < \theta_{\text{jet}} < 20^\circ$ .

by  $Q_1^2 Q_2^2 / W_{\gamma^* \gamma^*}^2$ . However, differences in the application of the cone jet algorithm may affect the results.

The forward jet cross section presented by H1 [36] is well described by an ordinary parton shower prescription including the possibility of having resolved photons. The criteria that the  $p_{\perp}^{\text{jet}}$  should be of the same order as  $Q^2$ , makes the scale choice crucial and  $\mu_5^2 = p_{\perp}^2 + Q^2$  is favoured by data, as concluded in [24]. With this experience we predict the forward jet cross section to be obtained at LEP. With more data accumulated and analyzed, the  $(p_{\perp}^{\text{jet}})^2/Q^2$  interval could be split into several subranges, which hopefully would help to discriminate between different scale choices.

Multiple interactions for the anomalous component are not yet included, and is not expected to be of same importance as in the VMD case. However, for low  $k^2$  fluctuations it may be important, especially for SaS 1D, and need to be investigated.

After this study of jet production by virtual photons it is natural to extend the modeling to low- $p_{\perp}$  events. Clearly, a smooth transition from perturbative to non-perturbative physics is wanted. One idea is to make use of a parameterization of the total  $\gamma p$  and  $\gamma\gamma$  cross section in terms of a pomeron and a reggeon exchange. Starting from the real-photon case, dipole dampening factors are introduced for the generalization to virtual photons. For example, the  $\gamma p$  cross section is divided into a VMD, an anomalous, a direct and a DIS  $\gamma^* q \rightarrow q$  process part. In the limit  $Q^2 \rightarrow 0$ , the first three event classes remain. On the contrary, when  $Q^2$  increases from zero to high  $Q^2$ ; the resolved processes dies out (as given by the dipole factors), the direct also drops and finally only the DIS process remain. At intermediate  $Q^2$  values, the direct processes and the DIS (+parton showers) process overlap, since, in some regions of phase space, they are equally valid descriptions of the same physics. It thus becomes necessary to avoid double-counting, e.g. by introducing Sudakov style form factors for the DIS process, suppressing those parton configurations covered by the direct processes. We intend to return to this issue in a future publication.

## Acknowledgements

We acknowledge helpful conversations with, among others, Jon Butterworth, Jiri Chýla, Gerhard Schuler, Hannes Jung, Leif Jönsson, Ralph Engel and Tancredi Carli.

## References

- [1] ZEUS Collaboration, M. Derrick et al., Phys. Lett. **B322** (1994) 287;  
H1 Collaboration, T. Ahmed et al., Nucl. Phys. **B445** (1995) 195.
- [2] G.A. Schuler and T. Sjöstrand,  
Nucl. Phys. **B407** (1993) 539; Z. Phys. **C73** (1997) 677.
- [3] G.A. Schuler and T. Sjöstrand,  
Z. Phys. **C68** (1995) 607; Phys. Lett. **B376** (1996) 193.
- [4] T. Sjöstrand, Computer Phys. Commun. **82** (1994) 74;  
<http://www.thep.lu.se/~torbjorn/Pythia.html>.
- [5] G. Marchesini, B.R. Webber, G. Abbiendi, I.G. Knowles, M.H. Seymour and  
L. Stanco, Computer Phys. Commun. **67** (1992) 465.
- [6] H. Kharraziha and L. Lönnblad, J. High Energy Phys. **03** (1998) 006.
- [7] G. Ingelman, A. Edin and J. Rathsman, Computer Phys. Commun. **101** (1997) 108.
- [8] R. Engel and J. Ranft, Phys. Rev. **D54** (1996) 4244.
- [9] H. Jung, Computer Phys. Commun. **86** (1995) 147.
- [10] M. Glück, E. Reya and M. Stratmann, Phys. Rev. **D54** (1996) 5515;  
D. de Florian, C. Garcia Canal and R. Sassot, Z. Phys. **C75** (1997) 265;  
M. Klasen, G. Kramer and B. Pötter, Eur. Phys. J. **C1** (1998) 261.
- [11] C.F. von Weizsäcker, Z. Phys. **88** (1934) 612.
- [12] E.J. Williams, Phys. Rev. **45** (1934) 729.
- [13] M. Klasen, G. Kramer and S.G. Salesch, Z. Phys. **C68** (1995) 113.
- [14] V.M. Budnev, I.F. Ginzburg, G.V. Meledin and V.G. Serbo,  
Phys. Rep. **15** (1975) 181.
- [15] G.A. Schuler, Computer Phys. Commun. **108** (1998) 279.
- [16] G. Bonneau, M. Gourdin and F. Martin, Nucl. Phys. **B54** (1973) 573.
- [17] S. Frixione, M.L. Mangano, P. Nason and G. Ridolfi, Phys. Lett. **B319** (1993) 339.
- [18] V.N. Baier, E.A. Kuraev, V.S. Fadin and V.A. Khoze, Phys. Rep. **78** (1981) 293.
- [19] G. Altarelli and G. Martinelli, Phys. Lett. **76B** (1978) 89;  
A. Mendéz, Nucl. Phys. **B145** (1978) 199;  
R. Peccei and R. Rückl, Nucl. Phys. **B162** (1980) 125;  
Ch. Rumpf, G. Kramer and J. Willrodt, Z. Phys. **C7** (1981) 337.

- [20] B.L. Combridge, J. Kripfganz and J. Ranft, Phys. Lett. **70B** (1977) 234;  
R. Cutler and D. Sivers, Phys. Rev. **D17** (1978) 196.
- [21] T. Sjöstrand, Phys. Lett. **157B** (1985) 321;  
M. Bengtsson, T. Sjöstrand and M. van Zijl, Z. Phys. **C32** (1986) 67.
- [22] M. Glück, E. Reya and M. Stratmann, Phys. Rev. **D51** (1995) 3220.
- [23] F.M. Borzumati and G.A. Schuler, Z. Phys. **C58** (1993) 139;  
M. Drees and R.M. Godbole, Phys. Rev. **D50** (1994) 3124.
- [24] H. Jung, L. Jönsson and H. Kuster, DESY 98-051 (hep-ph/9805396);  
DESY 99-028 (hep-ph/9903306), to appear in Eur. Phys. J. **C**.
- [25] B. Andersson, G. Gustafson, G. Ingelman and T. Sjöstrand,  
Phys. Rep. **97** (1983) 31.
- [26] CDF Collaboration, F. Abe et al., Phys. Rev. **D50** (1994) 5562.
- [27] S. Frixione, M.L. Mangano, P. Nason and G. Ridolfi, Nucl. Phys. **B431** (1994) 453;  
L. Apanasevich et al., Phys. Rev. **D59** (1999) 074007;  
G. Miu and T. Sjöstrand, Phys. Lett. **B449** (1999) 313.
- [28] T. Sjöstrand and M. van Zijl, Phys. Rev. **D36** (1987) 2019.
- [29] H1 Collaboration, S. Aid et al., Z. Phys. **C70** (1996) 17.
- [30] L. Lönnblad and M. Seymour (convenors),  
 *$\gamma\gamma$  Event Generators*, in “Physics at LEP2”, CERN 96-01,  
Eds. G. Altarelli, T. Sjöstrand and F. Zwirner, Vol. 2 (1996) 187.
- [31] ZEUS Collaboration, M. Derrick et al., Phys. Lett. **B384** (1996) 401.
- [32] J. Bromley et al.,  
HzTool — A Package for Monte Carlo Generator – Data Comparison at HERA,  
<http://dice2.desy.de/~h01rtc/hztool.html>
- [33] H1 Collaboration, C. Adloff et al., Phys. Lett. **B415** (1997) 418.
- [34] M. Glück, E. Reya and A. Vogt,  
Phys. Rev. **D46** (1992) 1973; Phys. Rev. **D45** (1992) 3986.
- [35] OPAL Collaboration, K. Ackerstaff et al., Z. Phys. **C73** (1997) 433.
- [36] H1 Collaboration, C. Adloff et al., Nucl. Phys. **B538** (1998) 3;  
H1 Collaboration, S. Aid et al., Phys. Lett. **B356** (1995) 118;  
ZEUS Collaboration, J. Breitweg et al., Eur. Phys. J. **C6** (1998) 239.